Vol. 34, No. 1, 2025

Machine
GRAPHICS & VISION

International Journal

Published by
The Institute of Information Technology
Warsaw University of Life Sciences – SGGW
Nowoursynowska 159, 02-776 Warsaw, Poland
in cooperation with
The Association for Image Processing, Poland – TPO

Basketball Player Target Tracking based on Improved YOLOv5 and Multi Feature Fusion

Jinjun Sun[1] and Ronghua Liu[2,*]

[1] *Department of Safety and Security, Zhejiang Posts and Telecom College, Shaoxing, China*

[2] *Department of Fundamental Discipline, Department of Physical Education,*
Shanghai University of Finance and Economics, Zhejiang College, Jinhua, China

[*] *Corresponding author: Ronghua Liu (liu2135173@163.com)*

Submitted: 18 Nov 2024 **Accepted:** 8 Jan 2025 **Published:** Mar 20, 2025

Abstract Multi-target tracking has important applications in many fields including logistics and transportation, security systems and assisted driving. With the development of science and technology, multi-target tracking has also become a research hotspot in the field of sports. In this study, a multi-attention module is added to compute the target feature information of different dimensions for the leakage problem of the traditional fifth-generation single-view detection algorithm. The study adopts two-stage target detection method to speed up the detection rate, and at the same time, recursive filtering is utilized to predict the position of the athlete in the next frame of the video. The results indicated that the improved fifth generation monovision detection algorithm possessed better results for target tracking of basketball players. The running time was reduced by 21.26% compared with the traditional fifth-generation monovision detection algorithm, and the average number of images that could be processed per second was 49. The accuracy rate was as high as 98.65%, and the average homing rate was 97.21%. During the tracking process of 60 frames of basketball sports video, the computational delay was always maintained within 40 ms. It can be demonstrated that by deeply optimizing the detection algorithm, the ability to identify and locate basketball players can be significantly improved, which provides a solid data support for the analysis of players' behaviors and tactical layout in basketball games.

Keywords: YOLOv5, object detection, action characteristics, recursive filtering, Mahalanobis distance, Hungarian algorithm.

1. Introduction

In the field of sports competition, basketball possesses the characteristics of high-speed confrontation and precise cooperation. In-depth analysis of athletes' performance is the key to improve team tactics and individual skills [24]. With the rapid development of computer vision and artificial intelligence technology, algorithms are gradually applied to target tracking (TT) of basketball players, showing great potential [4]. Through high-precision image processing and intelligent recognition technology, the algorithms are able to track key information such as the position, speed and movement trajectory of each player on the court in real time. This provides coaching teams with unprecedented game insight data [27]. This not only changes the way of training, but also promotes the scientific development of game strategies, enabling basketball to move towards a smarter and more efficient future in the wave of digitization.

In terms of target detection, Song et al. designed an intelligent recognition system combining multi-TT algorithm and YOLOv5 ware in order to solve the problem of fine target occlusion affecting helmet detection. The actual test results at a complex construction site indicated that the average accuracy of the intelligent recognition system was 94.5%, and the detection speed was up to 40 fps, which basically realized the real-time detection [21]. Zhan et al. improved the algorithm's target detection performance in UAV scenarios and chose to incorporate four methods to improve small target detection accuracy based on YOLOv5. The findings demonstrated that the model that combined the several improvement techniques not only significantly increased detection accuracy but also successfully decreased detection speed loss up to 55 fps [32]. Bharathi and Anandharaj developed a YOLOv5 multi-TT model that could detect, track and recognize individuals in order to help surveillance cameras measure social distances in road traffic videos. The results of the study found that the model achieved good results with 93% precision, 94% recall and 95% all class average precision for measuring social distance by object classification and localization in real time traffic surveillance video [1].

In terms of real-time tracking of motion trajectory, Hao et al. used the maximum interclass variance method for grayscale feature processing in an attempt to solve the efficiency problems of the current algorithms related to athlete detection and recognition. The study was based on Harris corner extraction algorithm and proposed multi-TT combining target corner features. The study showed that the algorithm performed well and had some practical effects [9]. Facchinetti et al. proposed an algorithm to automatically identify the active period of the sport using the tracking data of the athletes in basketball in order to obtain the accurate data of basketball between the course of the game and the intermission [5]. A basketball, a basket, and athletes were the feature extraction (FE) objects in Wang and basketball sports video TT method, which they combined with an upgraded gray neural network technique to better assess the condition of athletes in the video. The approach could successfully and accurately identify basketball movements, according to the findings of experimental testing, offering a new technique for basketball movement detection [25].

In summary, in the field of target detection and motion trajectory tracking, although some progress has been made in existing researches, such as improving detection accuracy and real-time performance, the detection efficiency is not high, and it is easy to miss detection in the case of target overlap and occlusion. Based on this, the research creates a new enhanced visual inspection algorithm (improved you only look once version 5, I-YOLOv5). To solve the missed detection problem caused by overlapping targets, a multi-attention module (AM) is innovatively added, and recursive filtering is used to predict the next position of the player, and then the prediction results are corrected by the actual situation.

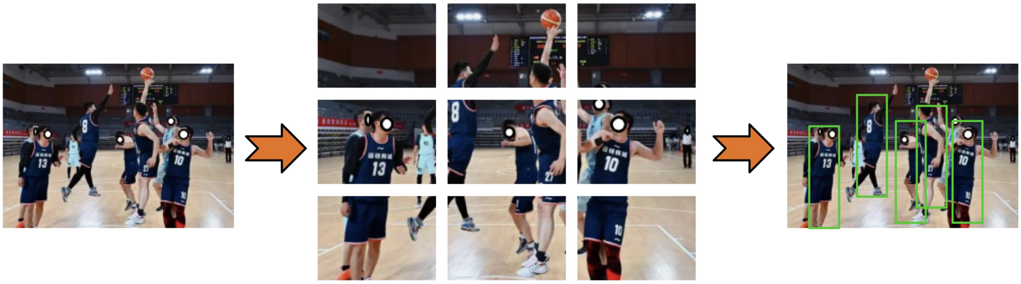

Fig. 1. Detection of basketball players by YOLOv5.

2. Methods

2.1. I-YOLOv5 algorithm for adding an attention module

With the increasing demand for sports event analysis and automated referee systems, computer detection plays an important role in real-time monitoring, action recognition, event detection, and content understanding. The traditional YOLOv5 algorithm is widely used in object detection due to its excellent real-time performance and high detection accuracy. However, the YOLOv5 algorithm is prone to inaccurate and undetected targets with small volume and high density, especially when dealing with complex backgrounds, athlete occlusions, and rapid movements, which may encounter problems such as missed detections, false detections, or unstable tracking [33]. The detection process of YOLOv5 algorithm for basketball players is shown in Figure 1. In this Figure, the YOLOv5 algorithm for the detection of the target, is required to cut the sports scene into multiple parts before detection, two for the absence of human body features of the block does not do the detection, which can reduce the algorithm's resource usage. However, for the basketball sports scene with more personnel, some basketball players only show part of their bodies due to the overlapping occlusion of personnel. The feature details are easily erased after the cutting process, resulting in a missed detection during the tracking detection process. For example. There should have been 7 people in the scene, but it is omitted to be detected as 5 people. For this reason, I-YOLOv5 is created by improving the YOLOv5 algorithm. In the I-YOLOv5 algorithm, a multi-AM is added to model the multi-dimensional situation simultaneously, and the information of different dimensions is fully displayed. The necessity of Global Average Pooling (GAP) lies in its ability to effectively aggregate feature map information into a global information representation, thereby reducing the number of model parameters, lowering computational complexity, and improving the model's generalization ability. The specific calculation method of GAP is to sum up all pixel values of the feature map and then divide by the total number of pixels. In the multi-AM, the introduction of GAP helps to enhance the model's attention to important features, improve the quality and diversity of feature representation. The formula for GAP in multi-AM is shown in Equation (1) [26].

$$\mathrm{CA}(T_x) = \frac{\sum_{a=0}^{K-1} \sum_{b=0}^{G-1} T_x(a,b)}{K \times G}\,, \tag{1}$$

where $\mathrm{CA}(T_x)$ represents the global information under the xth channel of the image, T represents the image, (a, b) represents the coordinate point position, a represents the width coordinate, b represents the height coordinate, K represents the image width, and G represents image height. The global information is obtained using only the basic features of the image without adding other information. To make the channel information richer and to obtain more representative global information, the 2D discrete cosine transform is combined to obtain channel information of more frequency bands, which is used to enrich the global information. The computation of the 2D discrete cosine transform spectrum is demonstrated by Equation (2) [31].

$$P_{k,g}^{\mathrm{2D}} = \sum_{k=0}^{K-1} \sum_{g=0}^{G-1} \mathrm{In}_{a,b}^{\mathrm{2D}} Q_{k,g}^{a,b}\,, \tag{2}$$

where $P_{k,g}^{\mathrm{2D}}$ represents the two-dimensional discrete cosine (2D-DC) transform spectrum under the height dimension frequency score g and width dimension frequency score k, $\mathrm{In}_{a,b}^{\mathrm{2D}}$ represents the two-dimensional input parameters, $Q_{k,g}^{a,b}$ represents the weight score, and D represents dimension. The weighting score is calculated as shown in Equation (3) [16].

$$Q_{k,g}^{a,b} = \cos\left(\frac{\pi g(a+0.5)}{G}\right) \times \cos\left(\frac{\pi k(b+0.5)}{K}\right)\,, \tag{3}$$

where both the height-dimensional frequency score g and the width-dimensional frequency score k are 0, and $Q_{k,g}^{a,b} = 1$. The relation between the 2D-DC transform spectrum and the GAP is shown in Equation (4).

$$P_{K_w}^{\mathrm{2D}} = \sum_{k=0}^{K-1} \sum_{g=0}^{G-1} \mathrm{In}_{a,b}^{\mathrm{2D}} = K \times G \times \mathrm{CA}(T_x)\,, \tag{4}$$

where T_x represents the x channel of image T. At this point the 2D discrete cosine transform spectrum and the global mean pool are in a positive correlation. The same applies for frequency scores of different dimensions, and feature information of many different dimensions can be calculated [22]. Figure 2 depicts the structure of the channel AM.

In Figure 2, the channel AM splits the image into slices of different parts. Equation (5) specifies how each slice's channel score is determined [20].

$$P^{e} = \sum_{k=0}^{K-1} \sum_{g=0}^{G-1} \mathrm{In}_{a,b}^{\mathrm{2D}} Q_{k,g}^{a,b} = \mathrm{2DT}\,, \tag{5}$$

where P^e represents the calculated channel score, 2DT represents the 2D-DC transform. The new merged channel is formed after integrating all the sliced processed channel scores. The merging process is shown in Equation (6) [8].

$$P_Z = \mathrm{cat}([P_1, P_2, \ldots, P_n])\,, \tag{6}$$

where P_n represents the sliced channel parameters of different layers, P_Z represents the merged channels, and $\mathrm{cat}(\cdot)$ represents the merge operation. The new channels are subsequently integrated with the slices to form a new channel AM [30]. The structure of another coordinate AM in the I-YOLOv5 algorithm is shown in Figure 3. In this Figure, in order to accurately capture the key information of the image in the width and height dimensions and encode the positions, it is necessary to apply special pooling operations to the input feature map (FM) along the horizontal and vertical directions, respectively. After determining the input parameter features, the special positions of all channels in the width direction are numbered. The vertical data of the channels are calculated as

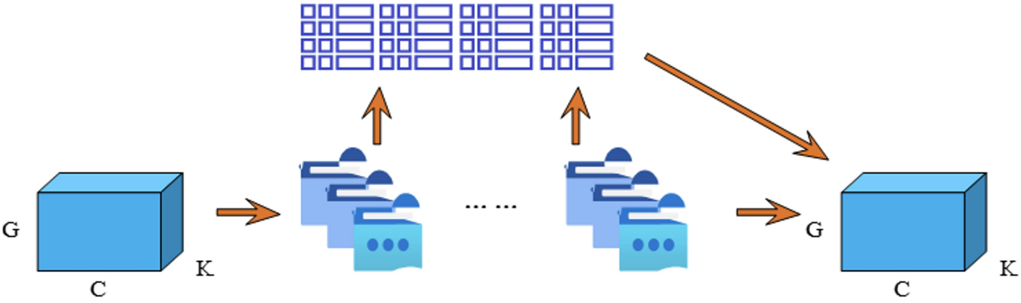

Fig. 2. Structure diagram of the channel attention module.

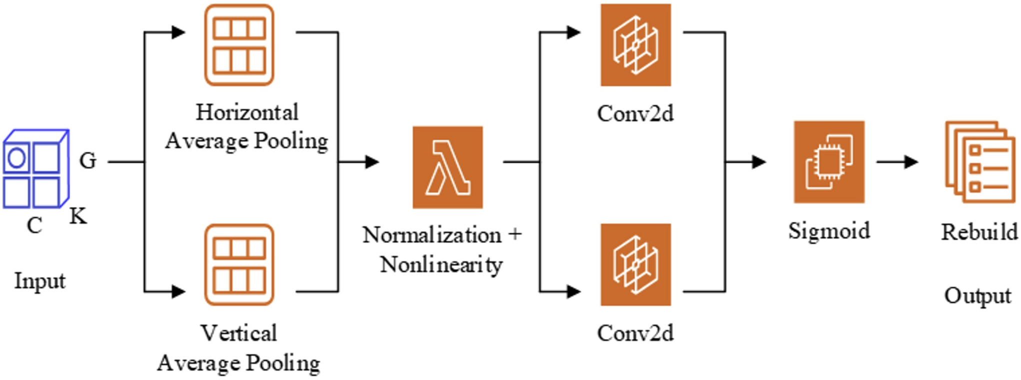

Fig. 3. Coordinate the structure of the attention module.

shown in Equation (7) [34].

$$O_x^{g_h} = \frac{\sum\limits_{0 \le b \le K_w} n_x(g_h, a)}{K_w}\,, \tag{7}$$

where $O_x^{g_h}$ represents the calculated value of vertical data with height g_h under the xth channel, (a, b) represents the point coordinates, K_w represents the width, and $n_c(g_h, a)$ represents the value of the image slice with height g_h and width coordinate a under the xth channel. Similarly, the horizontal data of the channel is calculated as shown in Equation (8) [18].

$$O_x^{k_o} = \frac{\sum\limits_{0 \le b \le G} n_x(b, k_o)}{G}\,, \tag{8}$$

where $O_x^{k_o}$ represents the calculated value of the horizontal data representing the width of k_o under the xth channel, G represents the height, and $n_x(b, k_o)$ represents the value of the image slice with width k_o and height coordinate b under the xth channel. These two specific operations are the core steps of feature processing. Integrating information along two different spatial dimensions, respectively, generates a pair of directionally sensitive FMs [29]. This process not only enhances the model's ability to capture long-range dependencies in one spatial dimension, but also subtly maintains precise spatial location details in the other dimension, thus optimizing the model's recognition and localization performance of the target object. With these two transformations, the model is able to analyze the spatial structure of the image or data more effectively and achieve more accurate target localization [11]. In order for the algorithm to obtain a faster running speed, the multi-AM and the coordinate AM are added to the I-YOLOv5 algorithm using a tandem approach. A brief description of the structure of I-YOLOv5 is shown in Figure 4. In this Figure the multi-AM and the coordinate AM also contain different component modules that implement the processing of the input parameters. The uniqueness of multi AM in I-YOLOv5 lies in its combination of Cross Stage Partial Network (CSP) module and Spatial Pyramid Pooling (SPP) module. The CSP module segments the input feature map, with one part passed directly and the other part merged after residual network processing to improve efficiency and feature learning. The SPP module captures multi-scale features and enhances the detection capability of multi-scale targets through parallel operations of multi-scale pooling kernels. While generating a coordinate description parameter through average pooling, the maximum pooling operation is used to obtain the maximum value of the coordinate parameter. Based on the different feature descriptions, the parameters are transferred to the data processing center module. By integrating the various parameters, the eligible feature values are produced, which enhances the I-YOLOv5 algorithm's detection performance. For the detection of basketball players, it is also necessary to input the specified features and the corresponding feature recognition structure. The current motion image recognition is only good at

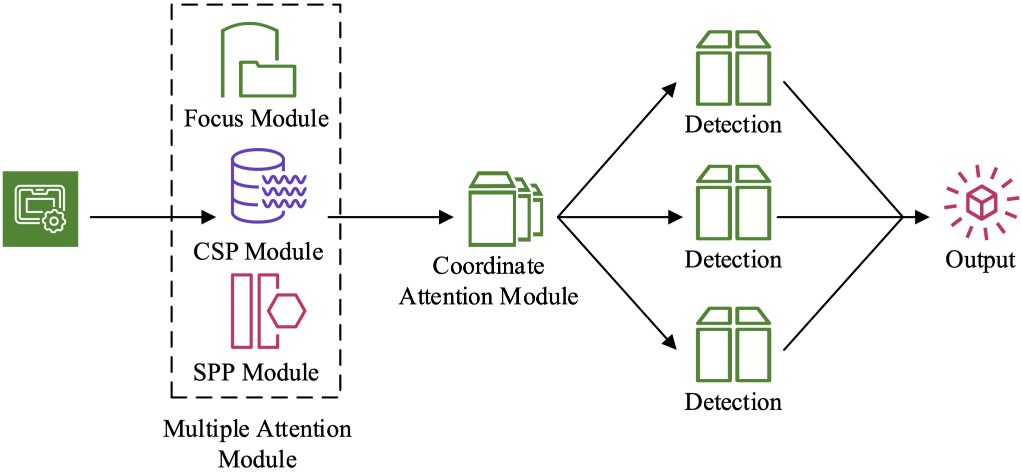

Fig. 4. I-YOLOv5 structure scheme.

tracking simple movements of a single target, while the movements of basketball players are often complex and variable. For this reason, a module for real-time discrimination of multiple features is also needed to improve the accuracy of detection.

2.2. Basketball player feature detection module

The key to more effectively deal with the complex and variable action recognition problem of basketball players is to construct an advanced detection module with adaptive ability and accurate target placement labeling in the image. Whether it is based on conventional algorithms or self-learning feature detection modules, the core of the effectiveness lies in whether or not the target is preset and accurately labeled in the recognition image. In the field of basketball player tracking, target detection, as a key technique, is directly related to the accuracy ratio (AR) of the tracking results [15]. Traditional target detection algorithms suffer from candidate region redundancy, high computation, low FE dependency, lack of robustness and fragmented detection process. These problems limit the detection efficiency and accuracy. In order to solve these problems, reduce computational burden and improve feature expression, fusion of detection links is needed to achieve global optimization. The two-stage target detection (TSTD) algorithm is an algorithm that provides high accuracy and is divided into two main processes. Firstly, it generates pending regions that may contain targets, and subsequently categorizes and edge-boxes recede from these pending regions. The whole process is shown in Figure 5 [10].

In Figure 5, the first stage of TSTD algorithm is the Regional suggestion network.

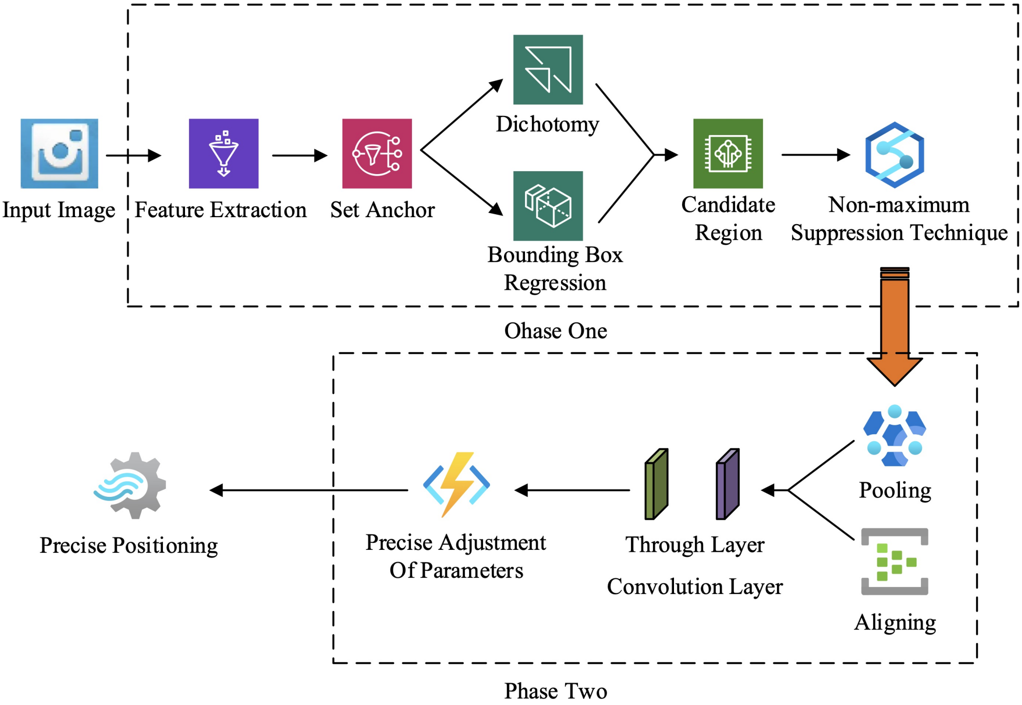

Fig. 5. Non-maximum suppression technique.

It is responsible for generating high-quality candidate regions from images [7]. The region suggestion network utilizes pre trained convolutional neural networks to extract feature maps and places anchor points of different sizes and proportions on them. By binary classification and bounding boxes (BOBs) regression, the region suggestion network identifies anchor points that may contain targets and uses non maximum suppression techniques to remove overlapping and low confidence candidate regions.

The second stage of TSTD algorithm is the Classification and regression networks. The task of this stage is to refine the candidate regions generated by the region suggestion network [13]. In this stage, the candidate regions are transformed into fixed size feature maps through region of interest pooling techniques, and then further feature extraction is performed using fully connected layers or convolutional layers. Finally, the network outputs the category probability and precise bounding box position for each candidate region. The architecture of the masked region-based CNN as a commonly used detection model in region suggestion networks is shown in Figure 6. The input image is first processed by the masked region-based CNN in Figure 6 before entering the

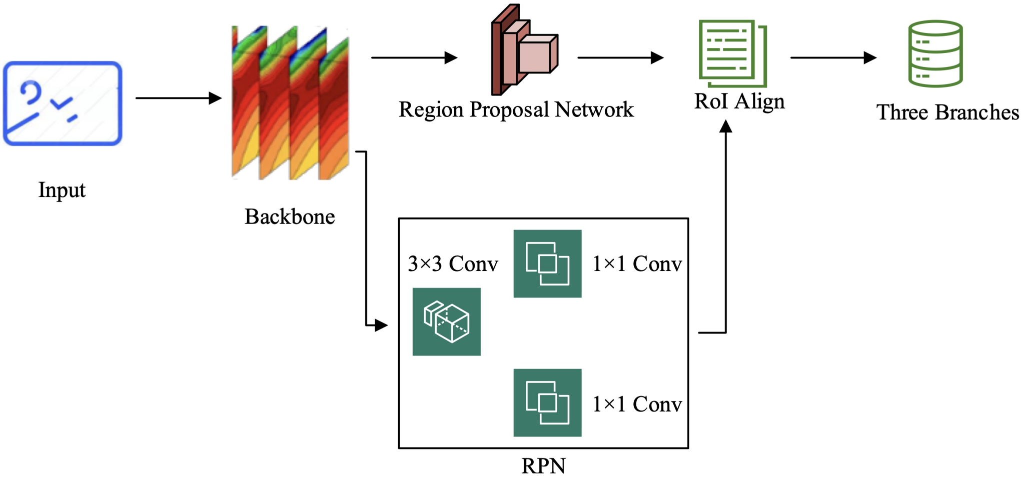

Fig. 6. Mask R-CNN structure.

classification model's backbone network. The backbone network is used to extract FMs with high semantic content by removing fully linked layers. The FM has a certain multiplicative reduction relation with the original image, and subsequently, the FM enters the core of the mask region-based CNN (MRCNN), i.e., the region suggestion network layer. The MRCNN generates candidate regions on the original map by means of small neural networks. Each FM pixel point corresponds to multiple candidate regions of the original map. The MRCNN then predicts the coordinate offsets of these candidate regions and the probability of whether they are foreground or not by convolution. The candidate regions are adjusted and filtered to select regions that are likely to contain objects. Finally, these candidate regions are accurately mapped and adjusted through the region of interest alignment layer. Candidate regions are mapped onto the FM by interpolation and uniformly resized. It is ensured that the candidate regions contain rich information of the original map to prepare for the subsequent fine recognition [19]. The loss function (LF) of the region of interest alignment layer is calculated as shown in Equation (9).

$$L_{\mathrm{ROI}} = L_c + L_b + L_m \,, \tag{9}$$

where L_{ROI} represents the LF of the region of interest alignment layer, L_c represents the classification LF, L_b represents the candidate region LF, and L_m represents the mask LF. The categorization LF mostly shows the discrepancy between the realistic categories and the predicted categories of the algorithm. The candidate region LF mainly represents the balance of the samples. The mask LF mainly indicates the loss value of the output value of each dimension. The control LF can effectively avoid the confusion of recognition of approximate features. The second categorization process of TSTD, for each category, the candidate box with the highest score is selected first [14]. Subsequently, the intersection ratio between the remaining candidate boxes and the highest scoring candidate box is calculated. If the intersection ratio exceeds a set threshold, the remaining candidates are removed, a process known as non-great value suppression. The purpose of non-great value suppression is to remove redundant candidate frames and ensure that only the best candidate frames are retained in each category. This step is repeated until all categories are traversed, ensuring that only one optimal candidate is retained for each category. After completing the non-extremely large value suppression, the remaining candidate boxes are further filtered. The remaining candidate frames in each category are then fine-tuned using multiple category-specific regressors designed to optimize their position and size. Eventually, each category will output a regression-corrected and highest-scoring edge box as the final detection result of the target in that category. As for the basketball players during the motion state process, modules with tracking functions are also added to the detection process because the people are constantly moving.

2.3. Tracking model based on multi-feature fusion algorithm

The athletes in basketball sports scenarios have a significant degree of appearance resemblance during the multi-person monitoring procedure. Moreover, their movements on the court are frequent and staggered, and once staggered movement or body overlap occurs, it is difficult for the tracking algorithm to accurately differentiate and recognize each athlete, which leads to the frequent problem of misidentification. For this reason, a tracking model for basketball players is constructed by combining multiple features and fusing them. The tracking model is based on a simple real-time tracking algorithm, and the next position of the athlete is judged by recursive filtering, which has a better prediction effect for the situation of having people in the shade [17]. Recursive filtering by analyzing the state parameters of the target at different moments for the corresponding next moment position judgment, in the output results will also be based on the real-time state of the target to correct the results [23]. The recursive filtering calculates the state of the target at different moments is shown in Equation (10).

$$Z_{t+1} = JZ_t + K_j I_{t+1} \, , \tag{10}$$

where Z_{t+1} is the state of the target at moment $t+1$, Z_t is the state of the target at the moment, J is the parameter switching matrix, K_j is the manipulation matrix, and I_{t+1} is the input moment value at moment $t+1$. The formula for recursive filtering to calculate the covariance moment values of the state parameters at different moments of the target after predicting the state parameters at different moments of the target is shown in Equation (11) [12].

$$X_{t+1} = JX_t \times J^T + V \, , \tag{11}$$

where X_{t+1} is the state parameter under moment $t+1$, X_t is the state parameter at moment t, J^T is the moment value operation coefficients at any moment, and V represents the noise moment value. Before the recursive filtering is about to output the predicted state, the output results are also corrected according to the target state parameters recognized at the current moment. The value-added calculation of recursive filtering is shown in Equation (12).

$$G_{t+1} = \frac{\overline{X}_{t+1} C^{T_r}}{(C\overline{X}_{t+1} C^{T_r} + \overline{V})} \,, \tag{12}$$

where G_{t+1} represents the recursive filtering under moment $t+1$, T_r represents any moment, $\overline{X}_{t+1}$ represents the detected real-time state parameters under moment $t+1$, C represents the detected moment value, and $\overline{V}$ represents the detected real-time noise covariance moment value. Equation (13), which calculates the best estimate of the target's state parameters, illustrates the process.

$$Z^R_{t+1} = \overline{Z}_{t+1} + G_{t+1}(g_{t+1} - C\overline{Z}_{t+1}) \,, \tag{13}$$

where Z^R_{t+1} represents the best estimate under moment $t+1$, $\overline{Z}_{t+1}$ is the detected real-time parameters under moment $t+1$, and g_{t+1} is the detected parameters under moment $t+1$. The corrected covariance moment values of the state parameters are calculated as shown in Equation (14).

$$\overline{X}_{t+1} = (1 - G_{t+1}C)\overline{X}_{t+1} \,, \tag{14}$$

where $\overline{X}_{t+1}$ represents the corrected state-parameter covariance moment values under moment $t+1$. Based on $\overline{X}_{t+1}$, the target-parameter position prediction under $t+2$ can be performed. When dealing with the multi-target following task, in order to efficiently approve the targets in consecutive frames, metrics such as intersection and merger ratios or feature similarity distances are often utilized to construct a loss moment value. The construction of this moment value lays the foundation for the subsequent data association step, and the core of constructing the loss moment value lies in transforming the multi-target following task into an optimal allocation problem. To handle such allocation difficulties, the Hungarian method is applied. Its basic principle is to work on a lossy moment value with equal rows and columns. Among them, each row of the moment values represents a goal in the previous moment, while each column corresponds to a goal in the next moment. The goal of the Hungarian algorithm is to find multiple elements of loss moments with the smallest loss without violating the "one row, one column" principle. Minimum loss elements are ideally 0, which represents no loss or the best match. The row and column indices of these elements directly indicate the correct correspondence of the targets in the preceding and following frames. With the Hungarian algorithm for loss moment values, the multi-objective following problem is transformed into a problem of finding the optimal set of elements in the loss moment values for a particular

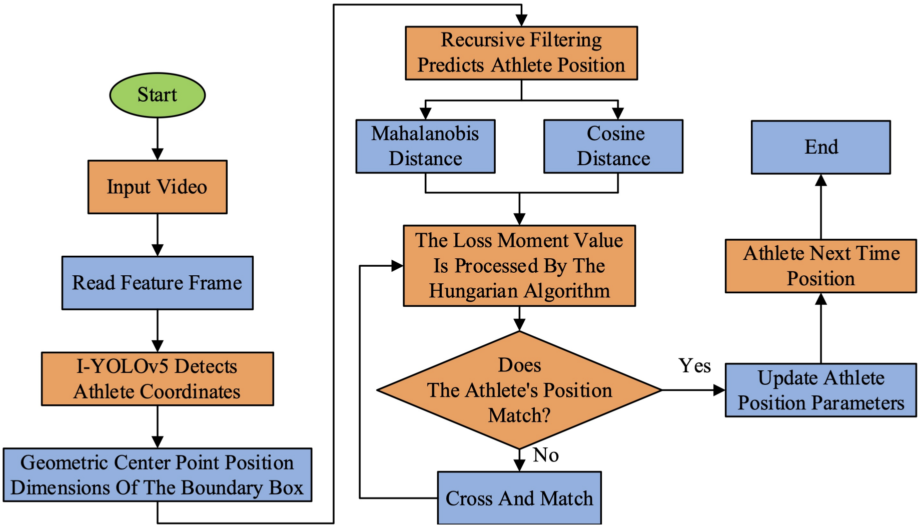
Start
Input Video
Read Feature Frame
I-YOLOv5 Detects Athlete Coordinates
Geometric Center Point Position Dimensions Of The Boundary Box
Recursive Filtering Predicts Athlete Position
Mahalanobis Distance
Cosine Distance
The Loss Moment Value Is Processed By The Hungarian Algorithm
Does The Athlete's Position Match?
Yes
No
Cross And Match
Update Athlete Position Parameters
Athlete Next Time Position
End

Fig. 7. Tracking model structure diagram of fusion algorithm.

pattern. These elements not only minimize the matching loss, but also ensure a one-to-one mapping between the targets in the front and back frames, resulting in an efficient and accurate TT association. An effective strategy in determining the final match is to combine the behavioral correlation with the appearance correlation, which is usually achieved by introducing a conditioning factor in the correlation evaluation model. The adjustment coefficient allows the system to flexibly adjust the weights between the two according to the actual application scenarios, thus calculating a more comprehensive and accurate athlete association. Equation (15) displays the correlation degree calculation.

$$D_{a_y,b_y} = k_t d^m(a_y, b_y) + (1 - k_t) d^y(a_y, b_y)\,, \tag{15}$$

where D_{a_y,b_y} represents the association of the b_yth athlete on trajectory a_y, k_t represents the moderating coefficient, d^m represents the horse distance, and d^y represents cosine distance. The final result can be obtained through the correlation degree, which is combined with the detection network to form the tracking model of the fusion algorithm to track the state of the basketball player at different moments. The whole flowchart is shown in Figure 7.

In the basketball sports video tracking model, the real-time position data of the athlete is initially extracted by the video detector. This includes the geometric center point position, the size of the BOB, and further extends to include the parameters of the velocity component. This comprehensive approach allows for a detailed portrayal of the athlete's motion state. Subsequently, recursion is used to predict the future position of the athlete and combined with the features extracted from the athlete behavior detection network to enhance the robustness of tracking. Next, the system constructs a comprehensive correlation matrix for evaluating the similarity between the detection and the existing trajectory by calculating the cosine similarity of the appearance features and making a prediction of the position. The relation between the tracked object and the detection is swiftly ascertained by using an efficient Hungarian algorithm to the problem of best matching of similar moment values. After a successful match, the tracking frame is directly output and the trajectory parameters are updated. For a failed match, the system tries to perform a secondary correlation by calculating the intersection and merger ratios to capture possible missed matches. For long time unsuccessful matching trajectories, the system will clean up to avoid resource waste. Meanwhile, the newly appeared unmatched detections are regarded as the starting point of the initial vectors to initiate the tracking. The whole process continues to iterate until all frames of the video are processed. In each iteration, the system dynamically adjusts the tracking strategy based on the latest information to ensure accurate tracking of athletes in complex sports scenes.

3. Results

3.1. Algorithm performance comparison

To ensure the efficiency of the tracking model, the operating system used for the experimental study is Windows 10, CPU is Intel Core i9-13900K @ 5.80 GHz, GPU is GeForce RTX 3070Ti, RAM is 32 G, programming language is Python 3.8, and the development environment is PyTorch l.5. The datasets used for the experimental training and validation process are Detectron dataset [6, 28] and SportsMOT dataset [2, 3]. The Detectron dataset supports multiple object detection algorithms, making it suitable for diverse algorithm testing and comparison. The SportsMOT dataset focuses on multi-target tracking in sports scenes, including sports such as basketball, soccer, and volleyball. It has two characteristics: fast and variable speed movement, as well as similar but distinguishable appearance, making it suitable for evaluating the performance of algorithms in complex sports scenes. The evaluation criteria used are AR, homing rate (HR), trace operation time (TOT) and frames per second (FPS). AR is mainly to judge the accuracy of the algorithm to detect the target, the higher means the more accurate. HR is mainly to judge the performance of the model's classifier, the higher it is the better the classification effect. TOT is to judge the algorithm's computing speed, the faster the better. FPS is to judge the rate at which the algorithm handles video tracking and localization, the higher the better. The comparison algorithms are the traditional YOLOv5 algorithm and simple online and realtime tracking (SORT). Figure 8 displays the LF decrease of each algorithm during the dataset's training procedure. On the Detectron dataset, the LF of the I-YLOLv5 algorithm stabilizes when the iterations reaches about 40,000,

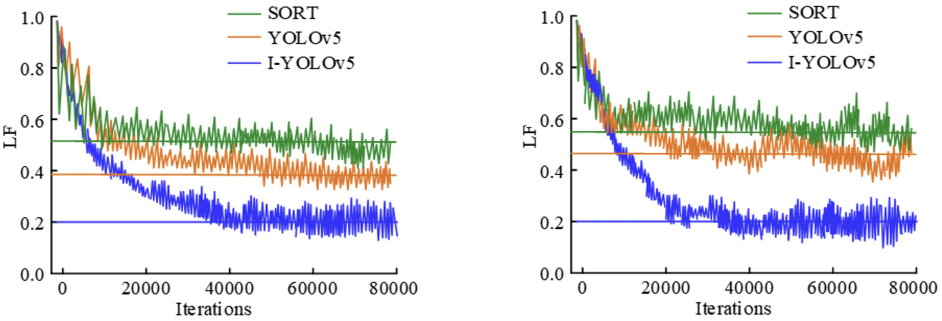

a Detectron.

b Iterations.

Fig. 8. Loss functions of various algorithms.

Tab. 1. Algorithm performance under different cutting ratio of image.

Model	SORT			YOLOv5			I-YOLOv5		
Size	AR (%)	HR (%)	TOT (s)	AR (%)	HR (%)	TOT (s)	AR (%)	HR (%)	TOT (s)
5 × 5	85.14	89.15	1.85	87.08	92.15	1.33	91.25	94.65	0.89
4 × 4	85.01	89.09	1.54	87.01	92.04	1.01	91.21	94.59	0.58
3 × 3	84.89	89.01	1.28	88.89	91.95	0.78	91.16	94.54	0.41
2 × 2	84.77	88.92	1.05	88.77	91.89	0.65	91.10	94.51	0.33
1 × 1	84.61	88.85	0.68	88.69	91.88	0.44	91.02	94.47	0.21

and the LF is 0.20. The LF of the YLOLv5 algorithm stabilizes when the iterations reaches about 50 000, and the LF is 0.38. The LF of the SORT algorithm stabilizes when the iterations reaches about 40 000 and the LF is 0.51. In Figure 8b, the SORT algorithm and the YOLOv5 algorithm have difficulty in reaching a more stable condition on the SportsMOT dataset, and the LF increases. Since the I-YLOLv5 algorithm adds multi-AM, the LF of the I-YLOLv5 algorithm can be stabilized quickly. Moreover, it can maintain around 0.2 in different datasets and the value of LF is the lowest among all the algorithms. By segmenting the image to different degrees, the detection of the segmented image by each algorithm is shown in Table 1. In this Table, the more the number of chunks of the image cut, the higher the AR and HR. As the chunks of the image becomes more, the running time of the algorithms becomes longer. After image cutting, the algorithm running time is mainly spent on the image merging process, while the coordinate AM of the I-YOLOv5 algorithm has the function of numbering each part of the image. This makes the I-YOLOv5 algorithm less affected by the image merging process, and the operation time is always kept within 1s. In the case where the image

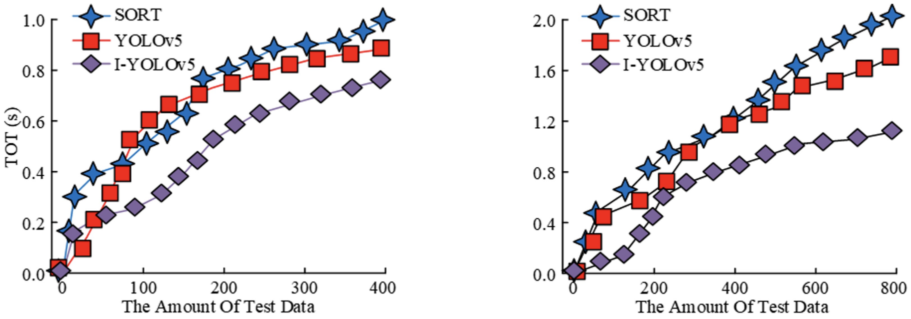

a Detectron.

b SportsMOT.

Fig. 9. Comparison of operation time of various algorithms.

is cut into 5 × 5, the running time of the I-YOLOv5 algorithm is 33.08% shorter than that of the traditional YOLOv5 algorithm. The SORT algorithm, on the other hand, has the worst performance situation, with the computation time directly exceeding 1s once the image has been cut. From this, it can be seen that the I-YOLOv5 algorithm, with its coordinate attention module, effectively reduces the impact of image merging on runtime. Even in scenes with many image cuts, the I-YOLOv5 algorithm still exhibits superior computational efficiency. The running time for each algorithm to complete the tracking on the Detectron dataset and the SportsMOT dataset is shown in Figure 9. In this Figure, the TT runtime of each algorithm on the Detectron dataset basically maintains a linear increase. Among them, the I-YOLOv5 algorithm has the shortest runtime, which is 21.26% lower than the second YOLOv5 algorithm runtime on average. In Figure 9b, the average running time of the I-YOLOv5 algorithm becomes significantly shorter when the amount of test data reaches 210 and no longer maintains the previous growth rate. This is because the TSTD module in the I-YOLOv5 algorithm makes it run faster during the training process, while the YOLOv5 algorithm and the SORT algorithm still maintain the same operation rate. From this, it can be seen that the I-YOLOv5 algorithm can stably track targets and maintain good stability even when facing large amounts of data. The algorithms are recognizing each frame of the video as an image while tracking the basketball players in the video data. The number of images per second that can be recognized by each algorithm is shown in Figure 10.

In Figure 10a, the FPS of the I-YOLOv5 algorithm on the validation dataset stays in a relatively stable state with an average value of 40, which is a 31.65% improvement over the traditional YOLOv5 algorithm. The SORT algorithm, on the other hand, has a worse performance situation, and SORT shows unstable FPS when processing some video clips with more complex personnel. In Figure 10b, affected by recursive filtering, the I-YOLOv5 algorithm got some learning during the testing process, with the ability to

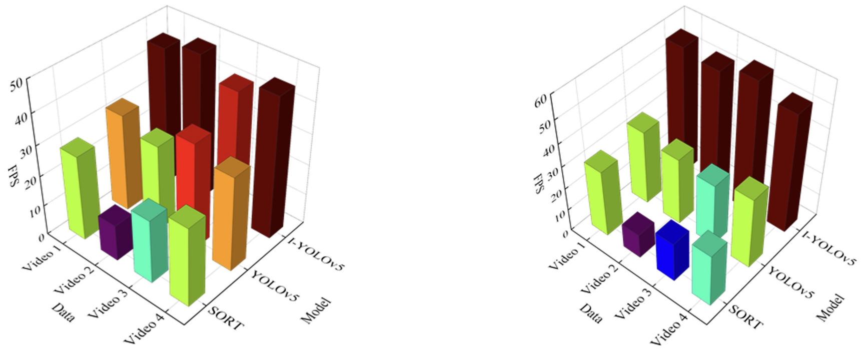

a Test.

b Validation.

Fig. 10. Various algorithms can recognize the number of images per second.

Tab. 2. Analysis results of target tracking performance of each algorithm.

Data set	Model	Image			Video		
		SORT	YOLOv5	I-YOLOv5	SORT	YOLOv5	I-YOLOv5
Detectron	Avg-AR [%]	85.41	92.51	98.98	78.54	88.15	97.21
	Avg-HR [%]	86.14	90.89	97.87	73.84	89.18	96.25
SportsMOT	Avg-AR [%]	84.21	91.58	99.01	76.58	87.51	98.65
	Avg-HR [%]	83.15	90.67	98.59	74.35	87.68	97.21

predict the next frame. The FPS of I-YOLOv5 algorithm has been improved somewhat during the validation process, with an average FPS of 49, which is 22.50% higher than the validation process.

3.2. Analysis of the effect of target tracking

In terms of performance, the I-YOLOv5 algorithm has been reflected in the comparison process in the previous section, while the specific tracking effect is mainly judged by AR and HR. In order to more accurately analyze the TT effect of basketball players for the three algorithms of SORT, YOLOv5 and I-YOLOv5, average accuracy ratio (Avg-AR) and average homing rate (Avg-HR) are used for comparison. Table 2 displays the outcomes of the comparison. The I-YOLOv5 algorithm has the highest Avg-AR and Avg-HR among all the algorithms both in image target detection and video TT process. During video TT on the SportsMOT dataset, the I-YOLOv5 algorithm has an Avg-AR of 98.65% and an Avg-HR of 97.21%. Due to the fact that video has more complexity than image, the algorithms have smaller AR and HR for tracking video targets than image

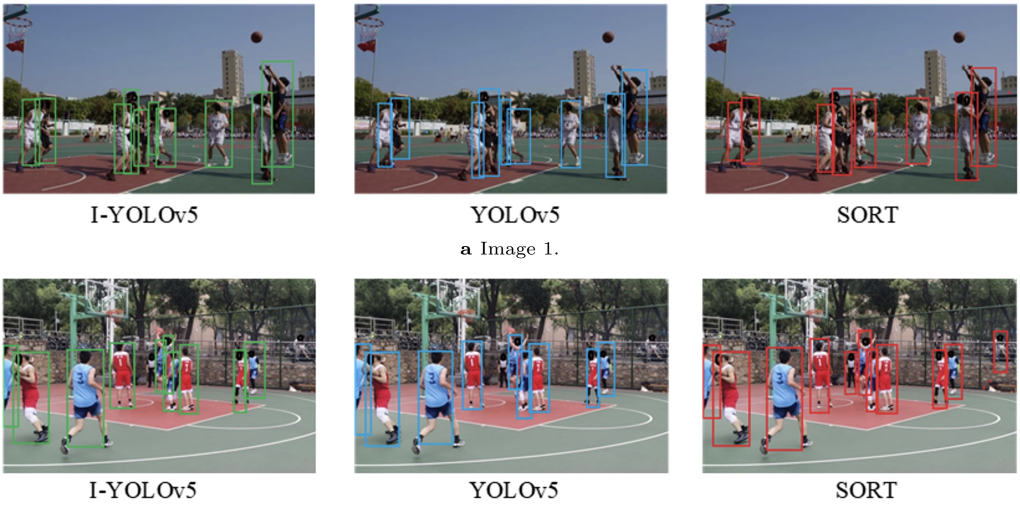

a Image 1.

b Image 2.

Fig. 11. Target tracking and recognition effect.

target detection. Whereas the I-YOLOv5 algorithm has a recursive filter prediction module, it still maintains high AR and HR during tracking video targets.

To show the tracking situation more intuitively, the target recognition effect is demonstrated. The recognition situation is shown in Figure 11. In this Figure, in the scenario facing personnel stacking, both SORT and YOLOv5 algorithms perform poorly with missed detection. The I-YOLOv5 algorithm, on the other hand, has precise localization of the personnel position due to the coordinate AM and avoids leakage detection due to personnel stacking. In Figure 11b, the SORT algorithm incorrectly treats the off-site personnel as the detection target. However, the I-YOLOv5 algorithm has more considerations for the correlation matching of the detection targets, so as to achieve the effect of detecting the targets accurately. For the TT situation of the video, a basketball player of a basketball game video clip is used as the tracking object, and the algorithm detects the number of people in each frame of the image to visualize the situation. The video is 30 FPS, 30 seconds in total, and the actual number of basketball players is 10. To simplify the data, the average value of target detection every 5 seconds is shown.

Table 3 displays the TT outcomes for each algorithm. The I-YOLOv5 algorithm maintains a more stable state during the TT process of the video. The number of target detections for each algorithm in the 11–15 seconds segment of the video is less than the actual number of athletes because some segments of the athletes during the game are out of the video range. The YOLOv5 algorithm appears to be unable to track the target

Tab. 3. Target tracking results of each algorithm.

Time [s]	Track effect evaluation index	SORT	YOLOv5	I-YOLOv5
0–5	Target detection average	7	9	10
	Missed average	3	1	0
6–10	Target detection average	7	9	10
	Missed average	1	1	0
11–15	Target detection average	6	7	8
	Missed average	2	1	0
16–20	Target detection average	5	7	10
	Missed average	5	3	0
21–25	Target detection average	8	9	10
	Missed average	2	1	0
26–30	Target detection average	9	10	10
	Missed average	1	0	0

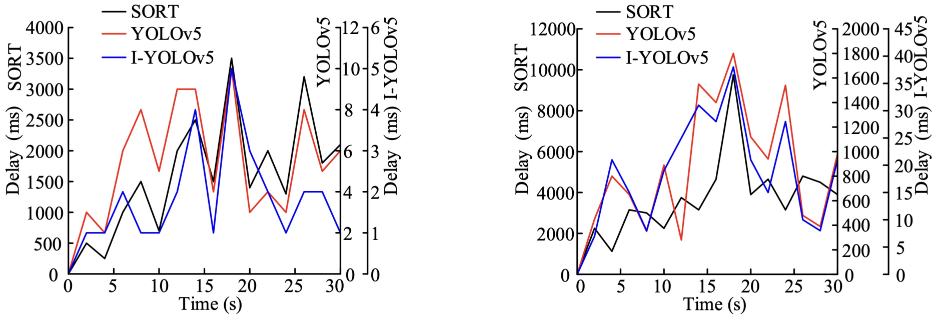

a 30 fps video. **b** 60 fps video.

Fig. 12. The delay of each algorithm in tracking different targets.

in the 16–20 seconds segment when some of the basketball players are moving faster. At this time, the fluctuation is more obvious, and there is only a complete number of targets detected by the I-YOLOv5 algorithm. From this, it can be seen that the I-YOLOv5 algorithm can stably track targets without any missed detections, and can fully monitor all basketball players. Ordinary online game videos of basketball tend to be in 30 or 60 FPS system. By using different algorithms for TT of the video, whether or not lagging occurs is an important indicator for judging whether the algorithms can perform online tracking. The delay of each algorithm in tracking different targets is shown in Figure 12. In this figure, both the YOLOv5 algorithm and the I-YOLOv5

Tab. 4. Application test results of I-YOLOv5 and Deep-EloU in basketball match

Index	I-YOLOv5	Deep-EloU
Average Delay [ms]	33	67
Avg-AR	99.08	97.54
Avg-HR	99.12	96.83
CPU usage [%]	26.54	35.67
Target loss	No	No

algorithm show a better steady state during video TT at 30 frames. The TT delays are all under 10 ms, while the SORT algorithm shows a delay of up to 3500 ms. In Figure 12b, under 60 frames video, the traditional YOLOv5 algorithm showed lagging phenomenon and appeared up to 1800 ms delay. However, the recursive filtering makes the I-YOLOv5 algorithm still maintain good stability during the video TT at 60 frames, with a delay of up to 45 ms. Therefore, the I-YOLOv5 algorithm can perfectly support online real-time tracking of basketball sports videos. To further analyze the performance of the I-YOLOv5 algorithm, the study also conducted a test comparison between the I-YOLOv5 algorithm and the Deep Expansion LoU (Deep IoU) algorithm in a practical application of a basketball game.

The test results are shown in Table 4. I-YOLOv5 performs better than Deep EloU in basketball games. The average latency of I-YOLOv5 is only 33 ms, much lower than Deep EloU's 67 ms, demonstrating faster response capability. In terms of accuracy and regression rate, I-YOLOv5 also leads Deep EloU with scores of 99.08% and 99.12%, respectively, surpassing Deep EloU's 97.54% and 96.83%, indicating higher tracking accuracy. Meanwhile, the CPU usage of I-YOLOv5 is relatively low at 26.54%, which is more energy-efficient than Deep EloU's 35.67%. Both did not experience target loss, ensuring the stability of tracking. It can be seen that I-YOLOv5 performs better than Deep EloU in terms of speed, accuracy, and resource utilization.

4. Conclusion

This research focuses on the tracking of athletes during basketball games. To ensure real-time tracking of the target, the YOLOv5 algorithm was improved by fusing the multi-feature detection module to form a new I-YOLOv5 algorithm. The image to be detected was first cut to some extent to remove redundant information. Subsequently, the target was recognized according to the feature parameters, followed by the prediction of the target's position in the next frame by calculating the cosine similarity. Finally, the prediction results were corrected by real-time images and the tracking results were output. The outcomes revealed that the I-YOLOv5 algorithm had a good performance.

The LF stabilized to 0.20 when the number of iterations reached about 40 000, and the images that could be processed per second was 49 on average. The target detection time of the I-YOLOv5 algorithm was 33.08% shorter than that of the conventional YOLOv5 algorithm when the image was cut to 5 × 5. The TT runtime of the I-YOLOv5 algorithm on the Detectron dataset was reduced by 21.26% compared to the traditional YOLOv5 algorithm. On the SportsMOT dataset, the I-YOLOv5 algorithm achieved an average accuracy of 98.65% and Avg-HR of 97.21%. The tracking latency of the I-YOLOv5 algorithm on 60 fps basketball sports videos was consistently maintained within 40 ms. In conclusion, the I-YOLOv5 algorithm exhibits a relatively short processing time and high accuracy. The I-YOLOv5 algorithm is capable of tracking the basketball player's target in real time on online videos and exhibits enhanced recognition of overlapping multiple targets. Furthermore, it is adaptable to the TT of a diverse range of basketball sports images or videos. While this research addresses the issue of tracking the movements of a basketball player, it does not extend to other types of targets. As such, additional studies are needed to examine this approach's effectiveness in various TT circumstances.

5. Authors' declarations

5.1. Conflict of interest

The authors have no conflict of interest to report.

5.2. Data availability

The information on the source of data is included in the manuscript.

References

[1] G. Bharathi and G. Anandharaj. A conceptual real-time deep learning approach for object detection, tracking and monitoring social distance using Yolov5. *Indian Journal of Science and Technology*, 15(47):2628–2638, 2022. doi:10.17485/IJST/v15i47.1880.

[2] Y. Cui, C. Zeng, X. Zhao, Y. Yang, G. Wu, et al. SportsMOT: A large multi-object tracking dataset in multiple sports scenes. In: *2023 IEEE/CVF International Conference on Computer Vision (ICCV)*, pp. 9887–9897. IEEE Computer Society, 2023. doi:10.1109/ICCV51070.2023.00910.

[3] Y. Cui, C. Zeng, X. Zhao, Y. Yang, G. Wu, et al. Sportsmot. GitHub, 2024. `https://github.com/MCG-NJU/SportsMOT`.

[4] P. T. Esteves, J. Arede, B. Travassos, and M. Dicks. Gaze and shoot: Examining the effects of player height and attacker-defender interpersonal distances on gaze behavior and shooting accuracy of elite basketball players. *Revista de Psicología del Deporte*, 30(3):1–8, 2021. `https://rpd-online.com/article-view/?id=466`.

[5] T. Facchinetti, R. Metulini, and P. Zuccolotto. Filtering active moments in basketball games using data from players tracking systems. *Annals of Operations Research*, 325:521–538, 2023. doi:10.1007/s10479-021-04391-8.

[6] R. Girshick, I. Radosavovic, G. Gkioxari, P. Dollár, and K. He. Detectron. GitHub, 2018. https://github.com/facebookresearch/detectron.

[7] C. Guo, M. Cai, N. Ying, H. Chen, J. Zhang, et al. ANMS: Attention-based non-maximum suppression. *Multimedia Tools and Applications*, 81(8):11205–11219, 2022. doi:10.1007/s11042-022-12142-5.

[8] M.-H. Guo, T.-X. Xu, J.-J. Liu, Z.-N. Liu, P.-T. Jiang, et al. Attention mechanisms in computer vision: A survey. *Computational Visual Media*, 8(3):331–368, 2022. doi:10.1007/s41095-022-0271-y.

[9] Z. Hao, X. Wang, and S. Zheng. Recognition of basketball players' action detection based on visual image and Harris corner extraction algorithm. *Journal of Intelligent and Fuzzy Systems*, 40(4):7589–7599, 2021. doi:10.3233/JIFS-189579.

[10] M. Hasanvand, M. Nooshyar, Moharamkhani, and A. Selyari. Machine learning methodology for identifying vehicles using image processing. *Artificial Intelligence and Applications*, 1(3):170–178, 2023. doi:10.47852/bonviewAIA3202833.

[11] L. He, J. C. W. Chan, and Z. Wang. Automatic depression recognition using CNN with attention mechanism from videos. *Neurocomputing*, 422(1):165–175, 2021. doi:10.1016/j.neucom.2020.10.015.

[12] Y. Ji, Z. Kang, and C. Zhang. Two-stage gradient-based recursive estimation for nonlinear models by using the data filtering. *International Journal of Control, Automation, and Systems*, 19(8):2706–2715, 2021. doi:10.1007/s12555-019-1060-y.

[13] M. Jin, H. Li, and Z. Xia. Hybrid attention network and center-guided non-maximum suppression for occluded face detection. *Multimedia Tools and Applications*, 82(10):15143–15170, 2023. doi:10.1007/s11042-022-13999-2.

[14] Z. Li, F. Liu, W. Yang, S. Peng, and J. Zhou. A survey of convolutional neural networks: Analysis, applications, and prospects. *IEEE Transactions on Neural Networks and Learning Systems*, 33(12):6999–7019, 2021. doi:10.1109/TNNLS.2021.3084827.

[15] Y. Liu, L. Geng, W. Zhang, and Y. Gong. Survey of video-based small target detection. *Journal of Image and Graphics*, 9(4):122–134, 2021. doi:10.18178/joig.9.4.122-134.

[16] Y. Ma, N. Li, Zhang, S. Wang, and H. Ma. Image encryption scheme based on alternate quantum walks and discrete cosine transform. *Optics Express*, 29(18):28338–28351, 2021. doi:10.1364/OE.431945.

[17] J. Mao, Y. Sun, X. Yi, H. Liu, and D. Ding. Recursive filtering of networked nonlinear systems: a survey. *International Journal of Systems Science*, 52(6):1110–1128, 2021. doi:10.1080/00207721.2020.1868615.

[18] Z. Niu, G. Zhong, and H. Yu. A review on the attention mechanism of deep learning. *Neurocomputing*, 452(1):48–62, 2021. doi:10.1016/j.neucom.2021.03.091.

[19] J. Ren and Y. Wang. Overview of object detection algorithms using convolutional neural networks. *Journal of Computer Communications*, 10(1):115–132, 2022. doi:10.4236/jcc.2022.101006. https://www.scirp.org/journal/paperinformation?paperid=115011.

[20] A. Rizaldy, P. Ghamisi, and R. Gloaguen. Channel attention module for segmentation of 3d hyperspectral point clouds in geological applications. *International Archives of the Photogrammetry, Remote Sensing and Spatial Information Sciences*, 48:103–109, 2024. doi:10.5194/isprs-archives-XLVIII-2-W11-2024-103-2024.

[21] H. Song, X. Zhang, J. Song, and J. Zhao. Detection and tracking of safety helmet based on DeepSort and YOLOv5. *Multimedia Tools and Applications*, 82(7):10781–10794, 2023. doi:10.1007/s11042-022-13305-0.

[22] R. Sun, J. Kuang, Y. Ding, J. Long, Y. Hu, et al. High-efficiency differential single-pixel imaging

based on discrete cosine transform. *IEEE Photonics Technology Letters*, 35(17):955–958, 2023. doi:10.1109/LPT.2023.3286105.

[23] H. Tan, B. Shen, and H. Shu. Robust recursive filtering for stochastic systems with time-correlated fading channels. *IEEE Transactions on Systems, Man, and Cybernetics: Systems*, 52(5):3102–3112, 2021. doi:10.1109/TSMC.2021.3062848.

[24] Z. Terner and A. Franks. Modeling player and team performance in basketball. *Annual Review of Statistics and Its Applications*, 8(1):1–23, 2021. doi:10.1146/annurev-statistics-040720-015536.

[25] T. Wang and C. Shi. Basketball motion video target tracking algorithm based on improved gray neural network. *Neural Computing and Applications*, 35(6):4267–4282, 2023. doi:10.1007/s00521-022-07026-6.

[26] W. Wang, S. Wang, Y. Li, and Y. Jin. Adaptive multi-scale dual attention network for semantic segmentation. *Neurocomputing*, 460(1):39–49, 2021. doi:10.1016/j.neucom.2021.06.068.

[27] Y. Wu, D. Deng, X. Xie, M. He, J. Xu, et al. Obtracker: Visual analytics of off-ball movements in basketball. *IEEE Transactions on Visualization and Computer Graphics*, 29(1):929–939, 2022. doi:10.1109/TVCG.2022.3209373.

[28] Y. Wu, A. Kirillov, F. Massa, W.-Y. Lo, and R. Girshick. Detectron2. GitHub, 2019. `https://github.com/facebookresearch/detectron2`.

[29] J. Xu, B. Ai, W. Chen, A. Yang, P. Sun, et al. Wireless image transmission using deep source channel coding with attention modules. *IEEE Transactions on Circuits and Systems for Video Technology*, 32(4):2315–2328, 2021. doi:10.1109/TCSVT.2021.3082521.

[30] X. Yang, Y. Luo, M. Li, Z. Yang, C. Sun, et al. Recognizing pests in field-based images by combining spatial and channel attention mechanism. *IEEE Access*, 9(1):162448–162458, 2021. doi:10.1109/ACCESS.2021.3132486.

[31] M. C. Yesilli, J. Chen, F. A. Khasawneh, and Y. Guo. Automated surface texture analysis via discrete cosine transform and discrete wavelet transform. *Precision Engineering*, 77(1):141–152, 2022. doi:10.1016/j.precisioneng.2022.05.006.

[32] W. Zhan, C. Sun, M. Wang, J. She, Y. Zhang, et al. An improved Yolov5 real-time detection method for small objects captured by UAV. *Soft Computing*, 26(1):361–373, 2022. doi:10.1007/s00500-021-06407-8.

[33] G. Zhaoxin, L. Han, Z. Zhijiang, and P. Libo. Design a robot system for tomato picking based on yolo v5. *IFAC-PapersOnLine*, 55(3):166–171, 2022. doi:10.1016/j.ifacol.2022.05.029.

[34] X. Zhu, K. Guo, S. Ren, B. Hu, M. Hu, et al. Lightweight image super-resolution with expectation-maximization attention mechanism. *IEEE Transactions on Circuits and Systems for Video Technology*, 32(3):1273–1284, 2022. doi:10.1109/TCSVT.2021.3078436.

V3DI Ensemble Model for High-Accuracy Aerial Scene Classification

K Aditya Shastry* and Reshma Itagi

Department of Information Science, Nitte Meenakshi Institute of Technology, Bangalore, India

Corresponding author: K Aditya Shastry (adityashastry.k@nmit.ac.in)

Submitted: 14 Feb 2024 **Accepted:** 29 Nov 2024 **Published:** 27 Mar 2025

Abstract Aerial images are valuable for observing land, allowing detailed examination of Earth's surface features. As remote sensing (RS) imagery becomes more abundant, there is a growing need to fully utilize these images for smarter Earth observation. Understanding large and complex RS images is crucial. Satellite image scenery categorization, which involves labeling images based on their content, has diverse applications. Deep Learning (DL), using neural networks' powerful attribute learning capabilities, has made significant strides in categorizing satellite imagery scenes. However, recent advances in DL for scenery categorization of RS images are lacking. In our study, we employed three transfer learning (TL) models – VGG16, Densenet201 (D-201), and InceptionV3 (IV3) – for classifying aerial images. VGG16 achieved 94% accuracy, while D-201 and IV3 reached 97% accuracy. Combining these models into an ensemble (V3DI ensemble model) improved accuracy to an impressive 99%. This ensemble model combines individual models' classification decisions using majority voting. We demonstrate the efficiency of this approach by showing how ensemble classification accuracy surpasses that of training individual models. Additionally, we preprocess the dataset with a Gabor filter for edge enhancement and denoising to enhance the model's overall performance.

Keywords: aerial image classification, remote sensing, deep learning, transfer learning, ensemble learning.

1. Introduction

A key data source for terrestrial observation, remotely sensed imagery aids in measuring and observing comprehensive features on top of the earth's surface. The number of images is rapidly increasing, leading to a greater demand for research on how to efficiently produce and analyze the majority of these images captured through remote sensing (RS) technology for detailed Earth inspection. Therefore, it is crucial to be able to understand huge and intricate remotely sensed images. Recognizing scenes in aerial photography is a demanding but required task for effective image interpretation, making it a key study topic. Recent high-resolution benchmark data sets have been made widely accessible by researchers from various organizations for the scene classification of RS data. The practical applications of RS scene categorization in urban planning, the discovery of natural hazards, environmental tracking, vegetation mapping, and geospatial item detection have spurred a number of studies over the past few decades. Fig. 1 illustrates how to appropriately classify a scene using RS imageries and established semantic categories.

The purpose of RS image analysis is to visually inspect Earth's surface using data

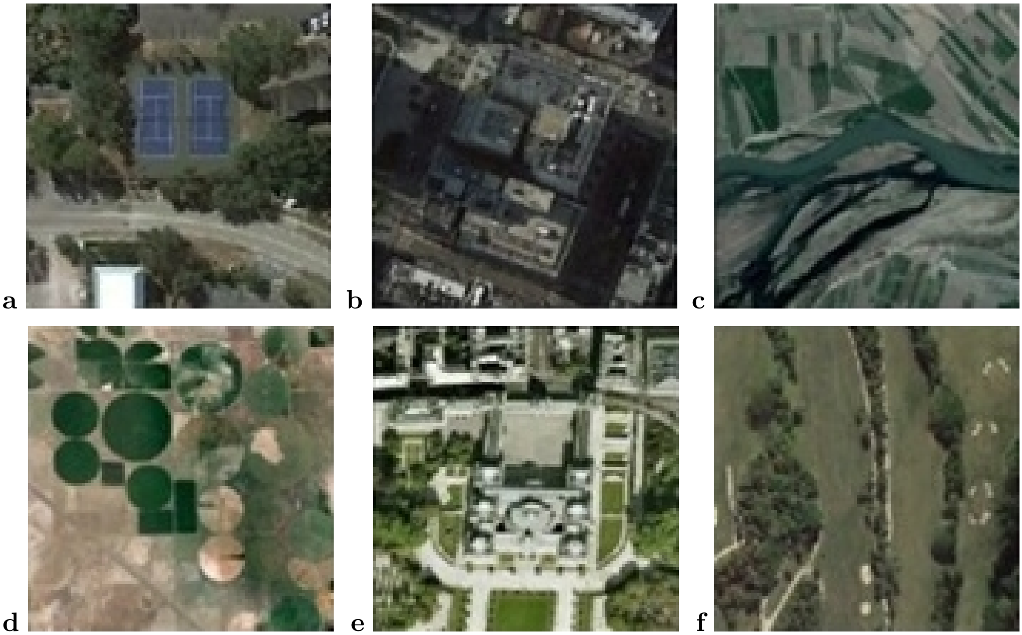

Fig. 1. Several scene images from the NWPU-RESISC45 dataset. (**a**) Tennis court; (**b**) commercial area; (**c**) river; (**d**) circular farmland; (**e**) palace; (**f**) golf course.

collected from satellites and unmanned aerial vehicles. Categorization of imagery is the backbone of visual recognition systems; after objects have been tagged with meaningful terms, they may be organized according to their conceptual significance. There are several applications of conceptual image organization in machine vision and imagery processing, including video synthesis, scenery evaluation, detecting objects, picture annotation, extraction, and content-driven image interpretation. By categorizing the pixels into different classes, image classification simplifies the data and makes it easier for users to analyze and understand spatial patterns, trends, and relationships. This information can be employed for several uses, like terrestrial usage and ground cover plotting, urban planning, agriculture monitoring, natural resource management, and environmental studies, among others.

In the past few decades, various academics have suggested multiple Deep Learning (DL) algorithms. These algorithms are used for categorizing scenes. They utilize freely available high-resolution standard data sources within this framework. While these models have demonstrated effective precision for smaller datasets, they encounter limitations in extracting features from high-resolution data. Our observation reveals that architectures enhanced with Gabor layers consistently improve robustness over regular models and maintain high generalization performance in tests. To determine the optimal ensemble learning approach, we train multiple Convolutional Neural Network (CNN) models on aerial datasets preprocessed with Gabor filters. Subsequently, we combine these models by averaging their predictions, resulting in improved accuracy. It is through this combination of predictions that we achieve the benefits of ensemble learning. Our research aims to develop an ensemble DL model capable of categorizing and labeling pixels or groups of pixels in satellite or aerial images based on their spectral values. Key objectives include identifying the most suitable pre-trained DL models for image classification based on previous research, constructing predictive models to extract features from high-resolution data and interpret complex patterns and information within the images, and converting raw data into more meaningful information applicable to various applications.

Transfer Learning (TL) involves applying skills learned from previous tasks to a new model for a different task. In deep learning, pre-trained networks are the core form of TL. There are two popular approaches: enhancing pre-trained models and using them as attribute extractors. The idea behind using pre-trained models as attribute extractors is to utilize the parent model with fresh data, replacing only the model's top layer while keeping its weights constant during training. Our research introduces a new framework that combines TL techniques and an ensemble method for Remote Sensing (RS) imagery classification. This framework incorporates the majority voting method and spatial features of landslides to achieve automatic and accurate results. Various organizations have recently made high-resolution benchmark datasets widely accessible for RS data scene classification.

The three main contributions of our research are as follows:

- The proposed ensemble model consists of pre-trained networks like VGG16, InceptionV3, and DenseNet201 that are trained using the datasets RESISC45 and NWPU-RESISC45 to categorize the RS images more accurately. The dataset is preprocessed with a Gabor filter for edge enhancement and denoising. This aids in enhancing the model's general performance.
- Our research offers a thorough analysis of the latest advancements in this area. We examine current benchmark repositories which are easily available to the public and several deep feature learning-based TL algorithms.
- Finally, we evaluate a number of representative methods including the TL-based DL approach and usage of CNN models with different classifiers which were performed with different datasets

The remaining part of this paper is organized as follows. In Section 2 the relared work is discussed. In Section 3 we propose our solution to the aerial scene classification problem. The results of experiments are presented in Section 4. Section 5 concludes the paper.

2. Related work

This section gives a complete evaluation of the works encompassing a broad spectrum of relevant work in RS imagery categorization is presented including network architectures (traditional CNN; Fully Convolutional Networks, FCN; encoder-decoder, recurrent networks; attention models, and generative adversarial models). The characteristics, capabilities, and limitations of current DL models were examined, and potential research directions are discussed. Since RS gives us imagery that enables accurate measurement and study of the Earth's surface features, it is a vital data source for Earth observation. These remote-sensing images offer a wealth of information, allowing us to examine and study the intricate details of our planet's surface. A growing volume of software's use remote sensor pictures. Because of this, it is more important than ever to figure out how to effectively use expanding quantities of RS information for insightful earth observation. Therefore, it is crucial to comprehend large and intricate remote-sensing images. Images captured by satellite have a variety of applications. Advanced learning uses images or data that have been remotely acquired. Consequently, researchers are able to comprehend numerous facets of the relevant domains. The noise and blur present in such photographs is a severe disadvantage. Noise removal is therefore the primary and initial step in the learning of images. Various sounds are added to the images as an outcome of the surroundings, such as particles in the sensor devices, light attenuation, haze, dust, etc. For professionals, pre-processing these photos is a difficult undertaking.

The various noise types [34] in the photos include Saltand-Pepper, Gaussian, Poisson noise, etc. Sudden and quick adjustments in the signal are what generate salt and pepper noise. Errors in the data flow cause this type of noise to arise. It is depicted by pixels of white and black that are sporadically present. The signal is equally spread out over the Gaussian noise. It has a Gaussian distribution and is statistical noise. A function with a probability density function that is identical to the Normal distribution is known as a Gaussian distribution. Each point's vibration operates independently of pixel value intensity. Poisson noise occurs when there aren't enough samples collected by the sensor to generate visible statistical data. Shot noise seems to be present in varying quantities, unlike light and electric current. Only a few of the numerous industries that have effectively exploited RS of images include classification and change detection. Nevertheless, RS image processing involves a few pre-processing processes in addition to categorization and change detection, and it also largely relies on the approach used. Because of this, the RS group is always trying to get better at areas like pre-processing, segmentation, and classification through the use of RS methodologies. The DL (DL) community has long used neural networks, which form the foundation of these techniques. Prior to the development of DL models, ensemble classifiers, including random forests (RF) and support vector machines (SVM), had replaced neural networks as the primary focus in the area of RS for the purposes of picture categorization and additional jobs like change detection. Due to its ease of use (e.g., being largely unaffected by classification parameter sensitivity) and typically high accuracy, SVM has grown in favour (Giorgos Mountrakis, 2011) [26].

While RF acquired popularity for a variety of factors including its capacity to manage high-dimensional data and perform effectively with limited training samples [3]. However, the growth of DL in more recent years has sparked a resurgence in interest in neural networks. DL algorithms have displayed outstanding performance at many image analysing tasks, including object identification, scene classification, and “land use and land cover” (LULC) classification. Thanks to advancements in computer and remote monitoring satellite technology, the images now have better spatial resolution, texture information and appropriate processing techniques. Data from ”High Spatial Resolution RS” (HSRRS) was utilized effectively for information extraction, categorization, and object identification [22,23,37]. Numerous HSRRS images have been collected recently, and key work has been done in the domains of pattern recognition, LULC [2,7]. These methods begin by mining attributes from training information before creating a classification model to test on more data. Most of the recognition techniques are DL-based. DL performs better for target identification, object recognition, and classification. It was effectively used to extract abstract and semantic features [11,14,15,18,24,33,35].

CNNs are a popular DL technique and several CNN-based methods have been designed for Natural Language Processing (NLP), computer vision, processing of medical images, and processing of images from remote sensors [30]. These real-world examples showed that a network’s depth is crucial for the model since it allows it to extract more complicated characteristics when there are more layers. While a deep layered model will improve performance and require a small amount of training, deep CNN (DeCNN) models frequently need a large quantity of labelled data. Finding enough labelled data to train the DeCNN model for the HSRRS scene classification issue is challenging. Additionally, labelling the HSRRS data requires a lot of manpower and materials. When the amount of labelled data is insufficient, the trained DeCNN model will quickly exhibit an over-fitting issue. Many research investigations have proven that TL is effective in classifying and identifying objects from small-sized training records.

2.1. RS imagery scene categorization

- **Multilevel RS imagery scene categorization** An in-depth study has been conducted on the challenge of single-label photo categorization throughout the past few decades. However, because of the usage of the birds-eye imaging method, it is very typical in the actual world for several ground objects to show up in a satellite image. Due to this, single-label RS picture scene categorization hinders the ability to fully comprehend the complex information included in RS imageries. Despite recent research into multilabel satellite image scene classification [4,9,12,13,19,31,32], there are still a number of challenges that require to be resolved, including how to utilize the relationships between various labels, how to acquire more generally applicable discriminative characteristics, and how to construct sizable multilevel datasets for scene categorization.

- **Increasing the size of scene classification datasets** Every type of scene in every open-world scenario would be easily and accurately recognised by the ideal scene classification system. Recent scene classification algorithms are only potentially capable of classifying scenes which prevail in the training datasets because they are trained on a restricted number of datasets. Consequently, a convincing method for classifying scenes ought to appropriately classify a brand-new scene image. There are many fewer scene classes in the published datasets [24–26] than what people can differentiate. A normal deep CNN also has a myriad of criteria and a propensity to overfit the several thousand of training instances. As a consequence, it is very difficult to completely train a deep classification model using the scene classification records that are presently available. Most sophisticated scenery categorization procedures either use pre-trained CNNs as attribute miners or refine already-trained CNNs on the target records. Transfer techniques outperform a fully trained deep CNN model on target records with fewer types and examples, but it's not the best choice because, with enough training samples, the model can derive more specialized characteristics that can adapt to the target domain.
- **RS imageries** The category of RS imageries also includes photographs taken by astronomical satellites. These are employed in a variety of research on the environments of stars, planets, and galaxies. Galaxies' classification is another important topic of research. Astronomers are expected to need vast volumes of data for their studies. The categorization of this material as disks, bars, spirals, etc., will aid in the prediction of the evolution of the cosmos. The bars signify fully developed galaxies and the end of the academic years. In order to research the marine mammals that live in the deep ocean, RS photographs are also used to capture underwater scenes. Additionally, the investigation of oceanic sediment, seas, etc. makes use of these images. They are essential to the investigation of the occurrence of different species in the water. The Catalina survey and the Sloan Digital Sky survey both provide the galaxy view and astronomical data set as open source. These show a telescope-taken screenshot of the sky. Because of how blue and greyscale these telescopic views are, studying the sun and stars is difficult. To learn from these photos, several methods for mistake or noise removal must be incorporated. The categorization of these images is crucial to the domain of physics. Abraham et al. [1] employed the DNN architecture to categorize barred and non-barred galaxies. A 95% accuracy rate in categorizing the images was made possible by the neural network. There are still more advancements to be made in astronomical research, and they will shortly occupy a sizable developmental area. In other words, there hasn't yet been a comprehensive and methodical analysis of how DL is used in the domain of RS.

Although Zhu et al. [38] review was comprehensively compared to others, it focused on a few deserving (and more prevalent) sub-regions related to the domain of RS, such as 3D modeling applications, while disregarding numerous others, such as image classification applications. To fully and objectively comprehend the uses of DL for RS analysis, it seems necessary to conduct a greater amount of structured (i.e., quantitative) study. The number of publications on the subject is clearly growing at the moment. In a range of RS subfields, DL methods are used. For instance, scholars interested in both DL and RS can benefit from understanding the various applications of DL and the problems identified in such studies. Scene classification using remote-sensing data has many applications, which try to assign semantic categories to remote-sensing images based on their contents. Due to DNNs' capacity for feature learning, the categorization of remote-sensing picture scenes has attracted a great deal of attention. The study [6] offers a methodical assessment of DL algorithms for RS picture scenery categorization by encompassing a total of 160 articles, considering the field's quick evolution. The primary methods in categorizing and surveying RS images are auto-encoder-inspired techniques, CNN methods for classifying RS imageries, and "Generative Adversarial Network" (GAN) based methods. The efficacy of several sample techniques/algorithms on three frequently utilized standard datasets is also described in this study [6]. Specifications for RS imagery classification, and new and exciting research avenues are investigated.

2.2. Scene classification for RS images

An image captured by RS includes a range of ground objects. An industrial landscape might, for instance, include buildings, trees, and roads. Scene classification is much more challenging than object-oriented classification due to the diversity and complex spatial distributions of earth's surface objects that prevail in the scene. The classification of satellite picture sceneries has been the subject of extensive research in the past. To group RS imageries with sufficient precision, however, there hasn't yet been a method which can do it. The difficulty with within-class diversity is primarily due to the wide variations in how ground things look across semantic classes. It could be challenging to correctly classify scene images because ground objects frequently vary in design, structure, size, and distribution. Additionally, because of the imaging circumstances, that could be affected by factors like cloud, mist, weather, etc., when RS imageries are taken by aerial platforms, there can be evident variations in hue and rays strength observable inside the identical semantic class. Among the difficulties in classifying RS imageries are the significant within-class diversity and between-class similarity. Within-class diversity may also result from alterations in picture illumination. For instance, in Fig. 2, the physical characteristics of the scene labeled beach exhibit significant variations under various imaging circumstances. When it comes to between class similarity, the main problem is when the same items are present in various scene classes or there exists semantic

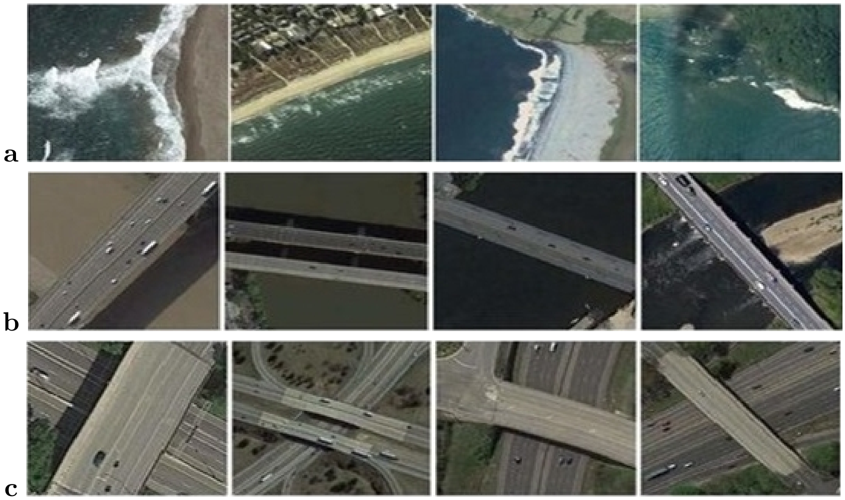

Fig. 2. Images with within-class diversity (**a**) and between-class similarity (**b**) and (**c**) used for scene classification. (**a**) Beach; (**b**) bridge; (**c**) flyover.

overlap between different scene types. As shown in Fig. 2, the bridge scene classes have structures similar to flyover scene classes.

So, both the bridge scenes and flyover scenes could contain identical objects including bridges, and share an abundance of semantic information. Moreover, interclass dissimilarity develops as a consequence of the ambiguous meaning of scene classes. Additionally, some complicated scenes share visual elements with one another. Consequently, it might be very challenging to differentiate between these scene classes. Unsupervised DL models that GANs have lately gained a lot of popularity (Goodfellow et al., 2014 [10]). The GAN has a framework consisting of a generative network and a discriminative network that are in competition with one another. The generative network's generated data and actual data are distinguished by the discriminative network. The generative network gains the ability to map from a hidden space to an interesting data distribution. It is trained with the intention of ”fooling” the discriminative network. A convolutional network is typically used by the discriminative network to generate odds. In a zero-sum game, the two networks attempt to optimise a distinct and antagonistic loss function (Oliehoek et al., 2017 [27]). GANs have been effectively utilized in numerous computer vision and image processing applications over the past three years. Based on a hierarchical law method, Classification Tree [16] is a multivariate, incremental, and evolutionary pattern detection system. The root, non-terminal, and terminal of a CT are its preceding components. It determines membership by frequently using binary dividing laws to segment a dataset. These laws are based on ”impurity” and are determined using mathematical techniques from the training data. A given node is perfect and there is no impurity present if the pixels that contain it belong to the same group. Unless the logical requirement is satisfied at a specific node, the left branch is selected; in that case, the right branch is noted. Until the terminal node is obtained or till the node is free, the loop continues to run. SVMs, among the most current advancements in AI, are based on ideas from statistical theory. Additionally, SVMs have outperformed the majority of other image classification algorithms in terms of classification accuracy. SVMs are binary classifiers that divide training data into two groups and maximize the difference between them using appropriate hyperplane division on multidimensional function space.

2.3. Recent study on DL techniques used for numerous applications

By comparing the overall accuracy of scene categorization of RS imagery methods using feature extraction done by pre-trained networks and classifiers, collected in Tab. 1, with proposed TL we can observe that the suggested technique of combining multiple pre-trained networks and forming an ensemble model achieves ideal classification performance in most classes.

3. Proposed methodology

It is challenging to classify remote data because of the intricacy of the environment, the variety of remote data, image processing, and classification techniques, to name just a few factors. The dynamic process of RS necessitates numerous picture analyses. Choosing a classification scheme, picking training objects, pre-processing the image, extracting features, putting appropriate classification methods into practice, postclassification storing, and accuracy evaluation are some of the essential actions in the classification of pictures.

TL is a DL technique that involves reusing a previously trained model. TL consists of re-using the knowledge gained from previously seen tasks to be applied to a newly created model in another task. In the context of DL, pre-trained networks are the basic form of TL. The two most popular approaches are using pre-trained models as feature extractors and fine-tuning pre-trained models. The main idea of using pre-trained models as feature extractors is to only replace the top layer of the source model and use it with the new data without updating the model weights during training. We will use this approach of incorporating prior knowledge taken from RS research literature in the creation of a customized high-performing DL model for satellite data tasks. The focus is to utilize a mildly complex and efficiently pre-trained model, learned from a large amount of reference information, such as ImageNet, and then “transfer” the learned information to a relatively simple task (in this study, extract features for scene classification) with a limited amount of information. Three features are very helpful in the transfer:

Tab. 1. Comparative analysis of the proposed method with other state-of-the-art techniques used for image scene classification.

Ref.	Method	Dataset	Accuracy	Description
[29]	DDIPNET DDIPNET+	Aerial Image Dataset-AID	(95.31±0.22)%	Applied the Discriminant Deep Image Prior Network and the Discriminant Deep Image Prior Network+, which combine Deep Image Prior and Triplet Networks learning strategies.
[36]	The suggested technique creates an SVM-based RS picture classifier	Aerial images from Pingshuo mining area, China	94.72%	After using the seven-layer CNN model, whose activation function makes use of the TReLU function, the three high-level image features are sequentially fused and fed into the SVM classifier.
[21]	TLDeCNN	High Spatial Resolution Remote Sensing Scenes (HSRRS)	96.1%-VGG19, 97.1%-ResNet50, 99.4%-InceptionV3	The three TL-DeCNN models TLVGG19, TLResNet50, and TLInceptionV3 are put forth for use in classifying HSRRS scenes in built-up urban regions.
[28]	CNN + PCA + SVM	UC Merced and WHU-RS	(98.26±0.40)%	With the extraction of features, a unique representation of the features was produced by combining the average pooling layer's features and the convolutional layer's PCA transformed features with SVM for classification.
[20]	DNN, i.e., CNN, CapsNet, SMDTR-CNN, and SMDTR-CapsNet	HSRRS	95.0%	Convolutional neural networks (CNN), capsule networks (CapsNet), the same model based on CNN with a different training rounding (SMDTR-CNN), and the same model based on CapsNet with a different training rounding are the four deep neural networks (DNNs) used. (SMDTR-CapsNet).
[25]	Applied DCNN Model	High resolution satellite image	92.0%	Multichannel water body detection network.
[17]	FeatSpace EnsNets and Avg EnsNets for Change Detection	ESA's Sentinel-1 and DInSAR processed georeferenced images	84.862%	Applied TL by fine-tuning neural networks (TLFT) is referred to as ”Feature space Ensembles of TLFE neural networks” (FeatSpaceEnsNets) and ”Average Ensembles of TLFE neural networks” (AvgEnsNets).
[8]	TL-DenseUNet	Remote Sensing Images dataset from NSFC, China	92.4%	There are two subnetworks in Applied TL DenseUNet. A transferring DenseNet pre-trained on three-band ImageNet images is one of them that the encoder subnetwork employs.

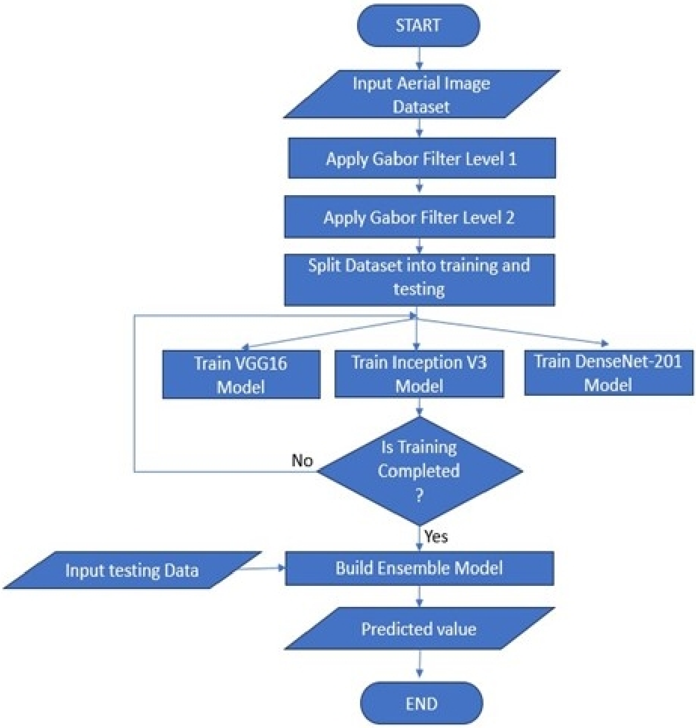

Fig. 3. Flowchart for the proposed classification procedure for RS images

- The advancement of the pre-trained model eases the process of getting rid of hyper-parameter tuning.
- The very first layers of a pre-trained model could be assumed to feature extractors, assisting in the separation of minimal features such as edges, colors, masses, shades, and surfaces.
- Because we accept that the subsequent layers complete the complicated identifying tasks, the objective framework may only need to retrain the next few layers of the pre-trained model.

The dynamic process of RS necessitates numerous picture analyses. Fig. 3 shows the flowchart of the classification procedure used for RS images.

It is challenging to classify remote data because of the intricacy of the environment, the variety of remote data, image processing, and classification techniques, to name just a few factors. Choosing a classification scheme, picking training objects, pre-processing the image, extracting features, putting appropriate classification methods into practice,

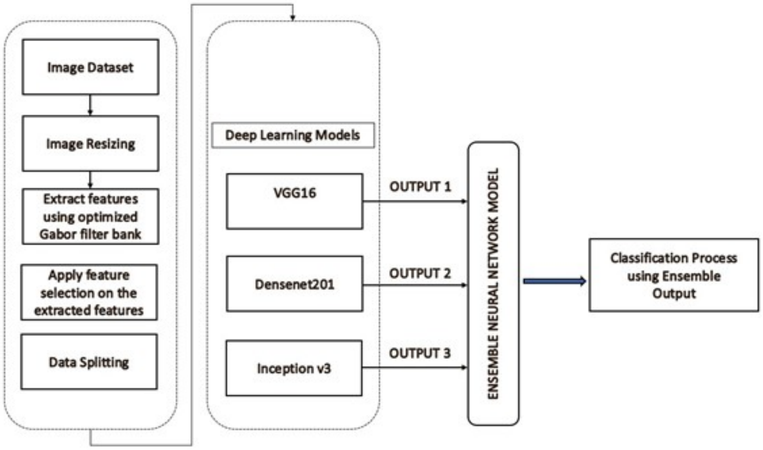
Image Dataset
Image Resizing
Extract features using optimized Gabor filter bank
Apply feature selection on the extracted features
Data Splitting
Deep Learning Models
VGG16
Densenet201
Inception v3
OUTPUT 1
OUTPUT 2
OUTPUT 3
ENSEMBLE NEURAL NETWORK MODEL
Classification Process using Ensemble Output

Fig. 4. Architecture of the proposed Ensemble Model for the automatic classification of RS images

post-classification storing, and accuracy evaluation are some of the essential actions in the classification of pictures. In this work, we stack multiple pre-trained CNN models on the ImageNet repository as an Ensemble Model and use them to train the aerial datasets. We train the ensemble model to get a high validation accuracy of around 98%. The output is obtained by combining the predictions of multiple trained models and averaging them. The proposed model is illustrated in Fig. 4.

The models are then combined by averaging, there taking a weighted average increases accuracy. The advantage of the ensemble learning method, which is improved predictive performance, is attained by combining the predictions. Ensemble techniques of stacking the model decisions rely on the assumption that different models will not make the same mistakes. In other words, given a set of diverse models, minimum of one will make the right classification. Fig. 5 demonstrates the data flow chart of the devised work.

TL has developed as a powerful method in the domain of DL, allowing us to leverage pre-trained models that were on large-scale datasets. By using TL, we could profit from the learned features of these models and adapt them to our specific task of aerial image classification. In this study, we employ three well-known TL models: VGG16, Densenet201, and InceptionV3. By combining the outputs of these models we aim to leverage their diverse strengths and improve the overall accuracy of aerial image classification. The findings and perceptions derived from this research will contribute to the advancement of automated analysis and understanding of aerial imagery, benefiting a wide range of applications and industries.

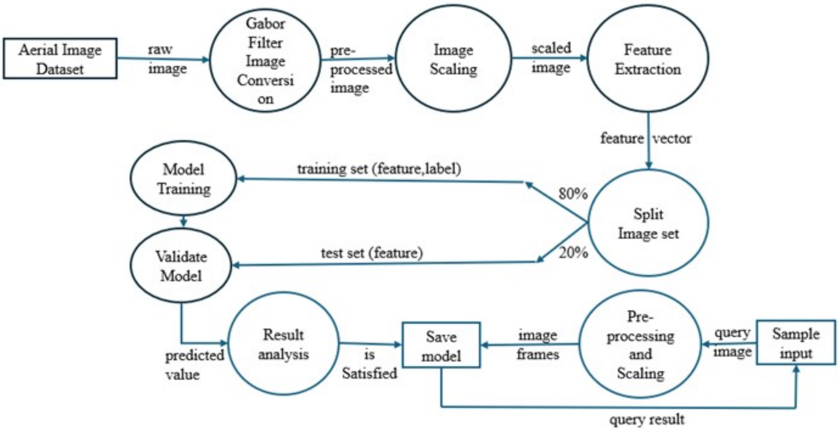

Fig. 5. Data flow plot of the devised work

3.1. Image acquisition and preprocessing

In this module, we will get the data from the online source. Further, we will resize the image for future use. Image resizing, also known as imagery scaling, is a geometrical operation that applies an image approximation technique to alter the scale of an image. By increasing or decreasing the pixel density of a target image, the aforementioned resizing operation modifies the final dimension of image information. Computers are able to perform computations on 0s and 1s and are unable to interpret images in the way that we do. We have to somehow convert the images to 0s and 1s for the computer to understand. The image will be converted to grayscale (range of gray shades from white to black) the computer will assign each pixel a value based on how dark it is. All the 0s and 1s are put into an array and the computer does computations on that array. We then feed the resulting array for the next step. It is common practice to first divide the dataset into two parts, the “Train” and the “Test”. Then, with the Test set put aside, the Train set is selected at arbitrarily from the Train dataset, and the remaining (100-X)% is used as the Validation set, with X resolved at a certain percentage (e.g., 80%). The algorithm is then developed and verified continually using these two sets. So we will follow the same method to prepare data for the training and testing phase. We are building our model by using the Ensemble network. Now that we’re done pre-processing, we can start implementing our individual deep-learning model. Max-pooling: A technique used to reduce the dimensions of an image by taking the maximum pixel value of a grid. This also helps reduce overfitting and makes the model more generic. After that, we add 2 fully connected (FC) layers. Since the input of FC layers should

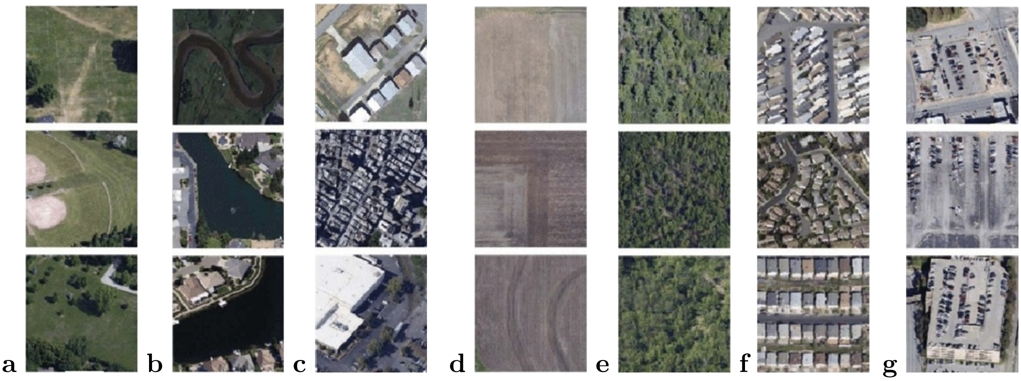

Fig. 6. Predefined classes from RSSCN7 dataset. (**a**) grass; (**b**) river; (**c**) industrial; (**d**) field; (**e**) forest; (**f**) residential; (**g**) parking.

be two-dimensional, and the convolution layer output is four-dimensional, we need a flattening layer between them. At the very end of the FC layers is a softmax layer. We are using 2 remote-sensing image datasets in this study.

- NWPU-RESISC45 Dataset: It is a 2017 dataset presented by Cheng, Han, and Lu [5]. It contains 31 500 256×256 RGB images split into 45 classes of 700 images each. It represents a comprehensive dataset regarding land use. NWPU-RESISC45 has a more diverse assortment of classes as well as more samples per class. The authors developed it in order to have both urban and rural classes as well as scenes classifiable by large features and small features alike. For all models, the input images are resized to 64×64×3, resizing from their original size of 256×256x3 while preserving the 3 RGB channels.
- RSSCN7 Dataset: It contains satellite imageries learned from Google Earth, which is originally collected for RS imagery categorization [39]. We conduct image synthesis on RSSCN7 to make it capable of the image inpainting task. It has seven classes: “grassland, farmland, industrial and commercial regions, river and lake, forest field, residential region, and parking lot”. Each class has 400 images, so the dataset comprises of 2 800 images. Samples of the dataset are shown in Fig. 6.

When processing images, the linear Gabor filter is just one of several methods used for things like feature extraction, examination of texture, boundary identification, etc. The band pass filtering devices, of which gabor filters are a subset, allow through only a narrow range of frequencies (or “band”) while blocking out all others. A Gabor filter can be viewed as a sinusoidal signal of particular frequency and orientation, modulated by a Gaussian wave. Gabor descriptor for an image is computed by passing the image through a filter bank of Gabor filters. Gabor filter represents a linear band-pass filter whose impulse response is defined as a Gaussian function modulated with a complex sinusoid. An artificial and actual part, signifying opposite directions, make up the filter's structure. The two components may be formed into a complex number.

$$g(x,y;\lambda,\theta,\phi,\gamma) = \exp\left(-\frac{x'^2+\gamma^2 y'^2}{2\sigma^2}\right)\cos\left(2\pi\frac{x'}{\lambda}+\phi\right), \tag{1}$$

where λ – wavelength of the sinusoidal component, θ – direction of the normal to the parallel bands of Gabor function, ϕ – phase balance of the sinusoidal procedure, σ – standard deviation of the Gaussian envelope, and γ – the Gabor function's ellipticity specified by the temporal dimension ratio.

The artificial and actual components of the "Gabor filter kernel" are applied to the image and the response is returned as a pair of arrays. An example of a linear filter is the "Gabor filter", which uses a sinusoidal plane waveform as modulation and a Gaussian base. Similar to how human vision represents frequencies and direction, the Gabor filter does the same. Gabor filters are appropriate for edge detection and texture classification. Attributes are mined from gray-scale character images by Gabor filters which are particularly devised from numerical data of character forms. An adaptive sigmoid module is employed to the outputs of Gabor filters to achieve better performance on low-quality images.

Gabor filters are used in texture analysis, edge detection, and attribute mining. When a Gabor filter is applied to an image, it delivers an optimal outcome at boundaries and at points where texture changes. Algorithm 1 illustrates the procedure used to generate Gabor layers for the input dataset.

In algorithm 1, two output directories (`gdir_1` and `gdir_2`) are defined to store the processed images. The function `create_dir()` is called to ensure that the required directories exist. This function is responsible for creating directories if they do not already exist. The algorithm iterates through each `label` in the input directory (`in_dir`). Each `label` corresponds to a category or class of images. For each `label`, the algorithm processes each image in the corresponding directory. If the image file does not conclude with `'.db'` (indicating it is not a database file), the following steps are performed:

- The path to the current image (`in_path`) and the output paths for the processed images (`out_path_1` and `out_path_2`) are defined.
- The image is read from `in_path`.
- Two Gabor kernels (`gabor_1` and `gabor_2`) are generated with specified parameters.
- The image is filtered using `gabor_1` to obtain `filtered_img_1`, and then `filtered_img_1` is further filtered using `gabor_2` to obtain `filtered_img_2`.
- The resulting filtered images (`filtered_img_1` and `filtered_img_2`) are saved to the corresponding output paths (`out_path_1` and `out_path_2`).

Once all images for a particular label have been processed, the algorithm ends.

Algorithm 1 Resource Allocation Algorithm

```
Initialize directories:
    Set gdir_1 as '/content/drive/MyDrive/Colab Notebooks/processed/gabor_1'
    Set gdir_2 as '/content/drive/MyDrive/Colab Notebooks/processed/gabor_2'
Create directories:
    Call create_dir(in_dir, out_dir, gdir_1, gdir_2)
Process images:
    for each label in the list of directories in in_dir do
        for each image_name in the list of files in the dir corresponding to label do
            if image_name does not end with '.db' then
                Set in_path as the path to the current image
                Set out_path_1 as the output path for the first Gabor filtered image
                Set out_path_2 as the output path for the second Gabor filtered image
                Read the image img from in_path
                Generate Gabor kernel gabor_1 with parameters:
                    Size: (18, 18)
                    Sigma: 1.5
                    Theta: $\pi/4$
                    Lambda: 5.0
                    Gamma: 1.5
                Filter img using gabor_1 to obtain filtered_img_1
                Write filtered_img_1 to out_path_1
                Generate Gabor kernel gabor_2 with the same parameters as gabor_1
                Filter filtered_img_1 using gabor_2 to obtain filtered_img_2
                Write filtered_img_2 to out_path_2
            end if
    end for
end for
```

Algorithm 1 essentially preprocesses a collection of images using Gabor filters. It enhances features in the images by applying Gabor filtering with two different kernels (gabor_1 and gabor_2). The administered imageries are subsequently kept in separate directories (gdir_1 and gdir_2). The final goal of this preprocessing step is to prepare the images for further processing or analysis, such as imagery categorization using TL models like VGG16, Densenet201, InceptionV3 and the ensemble model.

After preprocessing of the input dataset with Gabor filter the features in the image are enhanced and help in training the model to distinguish between pre-defined categories. Fig. 7 shows sample imageries which are acquired after preprocessing with the Gabor filter bank.

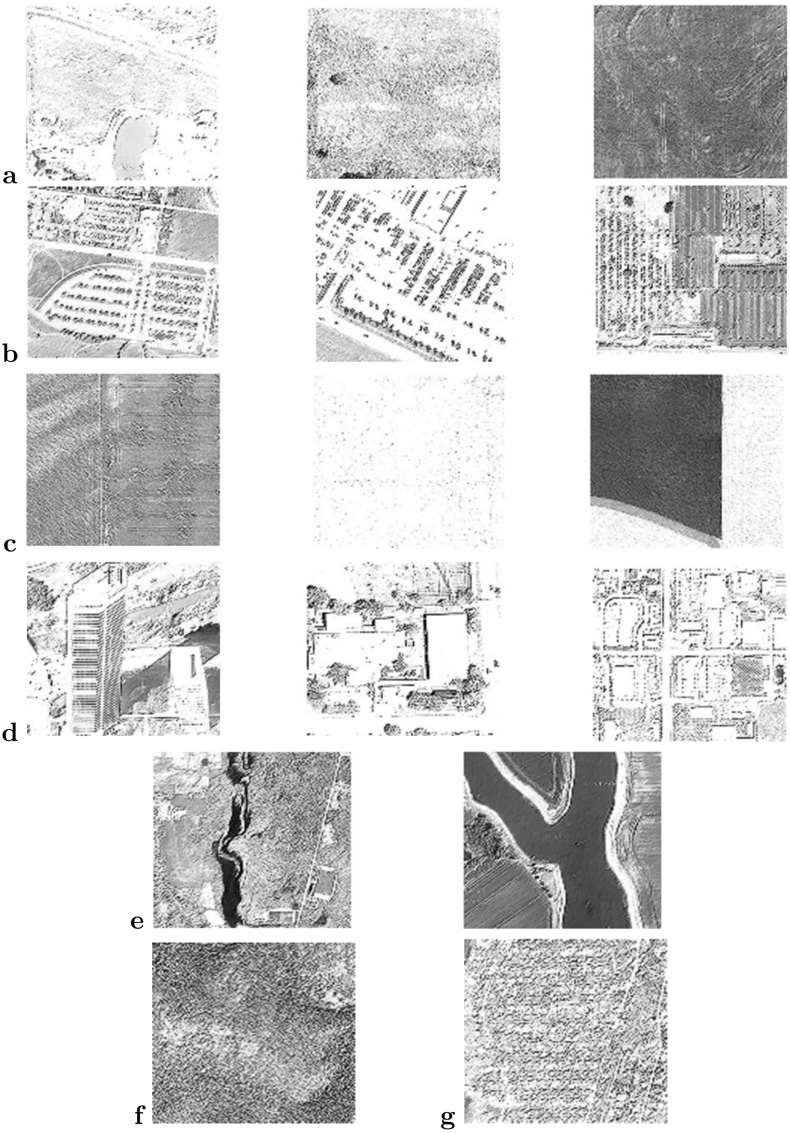

Fig. 7. Sample scene images categorized under different classes processed by the Gabor filter from the NWPU-RESISC45 dataset. (**a**) Grass; (**b**) parking; (**c**) field; (**d**) industry; (**e**) river lake; (**f**) forest; (**g**) resident.

3.2. Ensemble model

In machine learning, the ensemble approach refers to combining multiple models to improve the general performance of the prediction task. The fundamental notion in ensemble learning is that by combining multiple models, we can reduce the risk of individual models making errors and enhance the model's generalization performance. Ensemble methods can be applied to a wide range of machine learning algorithms, including decision trees, neural networks, and support vector machines. There are two key kinds of ensemble learning techniques: Bagging: Several models are trained independently on different subsets of the training data, and their predictions are aggregated by taking the average (for regression problems) or voting (for classification problems) of the outputs. Boosting: Here, the models are trained sequentially, and each novel model is trained to rectify the errors of the previous models. The notion is to create a strong model by combining many weak models. This system uses the Bagging ensemble approach. Ensemble learning integrates the forecasts from numerous neural network models to decrease the changes in forecasts and decrease generalization errors. The method starts by fine-tuning the 3 CNN models using the training data. By comparing models like VGG16, InceptionV3, and DenseNet201 and combining its output to get higher accuracy among the model predictions. To amalgamate the projected outcomes, the most straightforward approach is to compute the mean of the forecasts generated by the base classifiers.

4. Experimental results

This Section provides details concerning the results obtained during the classification of data with NWPU-RESISC45 and RSSCN7 datasets. It also summarizes the diverse measures utilized for performance evaluation. When utilizing DL methods for image classification, choosing the appropriate evaluation metrics is essential for determining which model to use, how to adjust the hyperparameters, whether regularization approaches are necessary, and other issues. Tab. 2 in page 43 summarizes the evaluation metrics for four models (Ensemble, InceptionV3, DenseNet201,and VGG16) across seven target classes (field, forest, grass, industry, parking, resident, and river lake).

The models generally exhibit high performance, with high precision, recall, and F1-scores for most classes. The Ensemble model achieves near-perfect scores for all classes, while the other models also show strong performance, although with some variations across metrics and classes. Overall, the models demonstrate accurate classification of the target classes, highlighting their effectiveness. A confusion matrix is a way to summarize the performance of a classification model by comparing its predictions with the actual values of a dataset. It is a square matrix where the rows correspond to the true or actual classes, and the columns correspond to the predicted classes. Accuracy is a measure that generally describes how the model performs across all classes. (number of all correct predictions divided by the total number of elements in the dataset).

Tab. 2. Classification report of pre-trained models with ensemble model.

VGG16 Model Results

Class	Precision	Recall	F1-Score	Support
Field	0.92	0.97	0.94	69
Forest	0.99	0.99	0.99	78
Grass	0.94	0.92	0.93	50
Industry	0.87	0.97	0.92	63
Parking	0.97	0.85	0.90	66
Resident	0.95	0.97	0.96	62
River lake	0.98	0.93	0.96	60

Densenet201 Model Results

Class	Precision	Recall	F1-Score	Support
Field	1	0.99	0.99	69
Forest	0.95	1	0.97	78
Grass	0.94	1	0.97	50
Industry	0.91	0.98	0.95	63
Parking	1	0.88	0.94	66
Resident	0.97	0.94	0.95	62
River lake	1	0.98	0.99	60

InceptionV3 Model Results

Class	Precision	Recall	F1-Score	Support
Field	0.92	1	0.96	69
Forest	1	0.97	0.99	78
Grass	1	0.96	0.98	50
Industry	0.98	0.92	0.95	63
Parking	0.93	0.97	0.95	66
Resident	0.95	0.98	0.98	62
River lake	0.9	0.93	0.97	60

Proposed Ensemble Model Results

Class	Precision	Recall	F1-Score	Support
Field	1	1	1	69
Forest	1	1	1	78
Grass	0.98	0.98	0.98	50
Industry	0.98	0.98	0.98	63
Parking	1	1	1	66
Resident	1	1	1	62
River lake	1	0.98	0.99	60

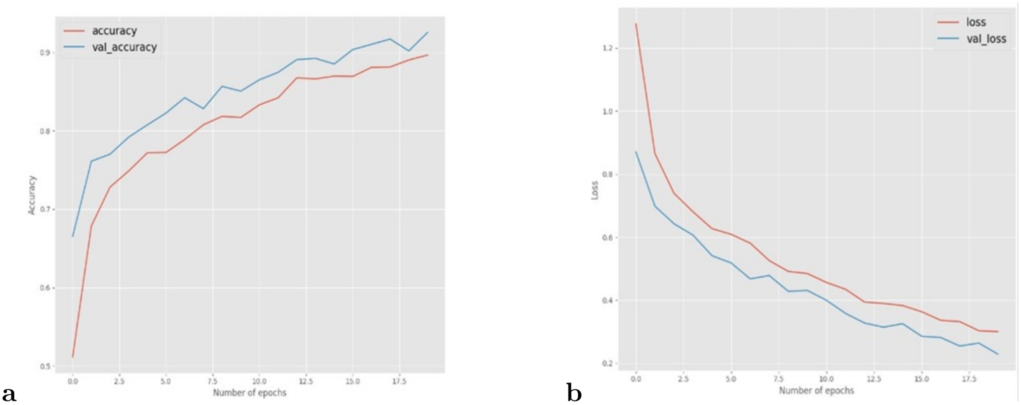

Fig. 8. Training model accuracy and loss plot graphs on RSSCN7 using using VGG16. (**a**) Accuracy plot graph; (**b**) Loss plot gragh.

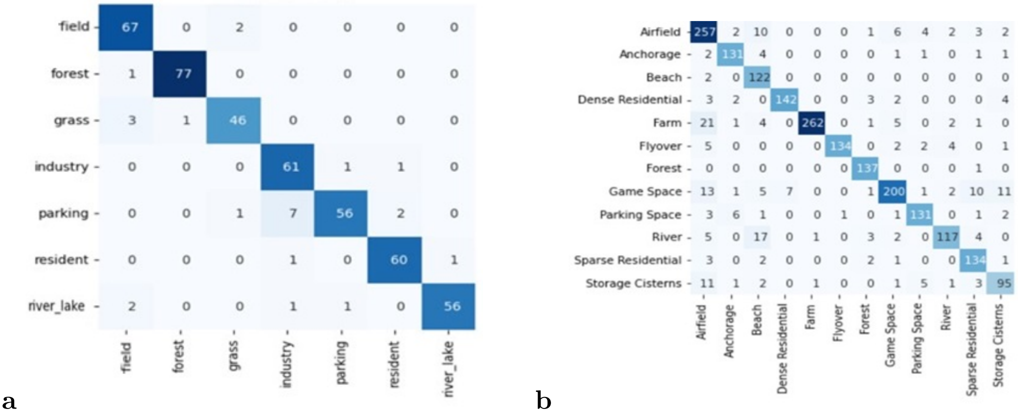

Fig. 9. VGG16 confusion matrix for the classification result for: (**a**) RSSCN7 dataset; (**b**) NWPU-RESISC45 dataset.

4.1. Experimental findings on the VGG16 Model

Fig. 8 demonstrates the training model accuracy and loss plot graphs on RSSCN7 using VGG16.

Fig. 9 shows the chart for the confusion matrix VGG16 model.

From the confusion matrix it can be concluded that this model is performing excellent. 448 photos from RSSCN7 dataset are provided in total and this model achieved 94% accuracy.

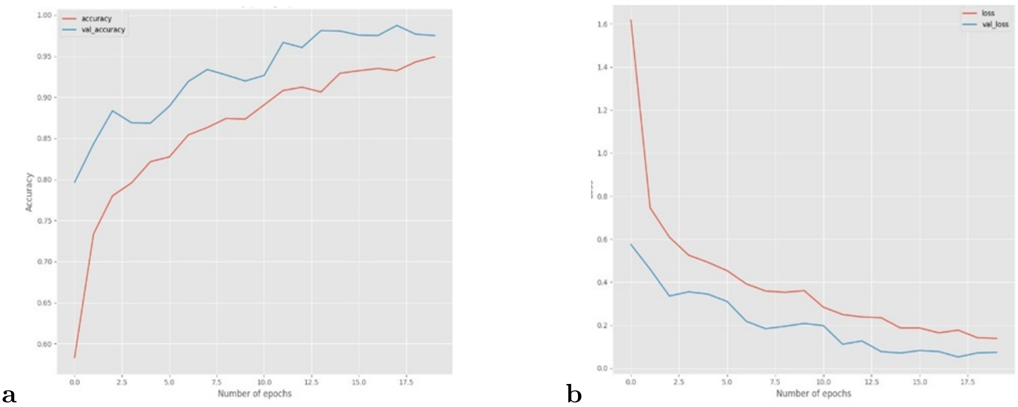

Fig. 10. Training model accuracy and loss plot graphs on RSSCN7 using DenseNet201. (**a**) Accuracy plot graph; (**b**) Loss plot gragh.

4.2. Experimental findings on the DenseNet201 model

Fig. 10 illustrates the training model accuracy and loss plot graphs on RSSCN7 using DenseNet201.

Fig. 11 displays the confusion chart for the Densenet201 model, illustrating its performance. The confusion matrix indicates that the model performs exceptionally well. A total of 448 photos from RSSCN7 dataset were evaluated, and the model achieved an impressive accuracy rate of 97%.

4.3. Experimental findings on the InceptionV3 model

Fig. 12 shows the training model accuracy and loss plot graphs on RSSCN7 using InceptionV3.

Fig. 13 illustrates the confusion matrix chart for the InceptionV3 model. Centered on the examination of the confusion matrix, it is evident that the model's performance is excellent. The dataset consisted of a total of 448 photos from RSSCN7 dataset, and the model achieved an impressive accuracy of 97%.

4.4. Experimental findings on the ensemble approach

An ensemble model of InceptionV3, Densenet201, and VGG16 was evaluated using a confusion matrix, represented by Figure 14. With 444 out of 448 images correctly predicted for the RSSCN7 dataset, the resulting accuracy is 99.11%, indicating high accuracy.

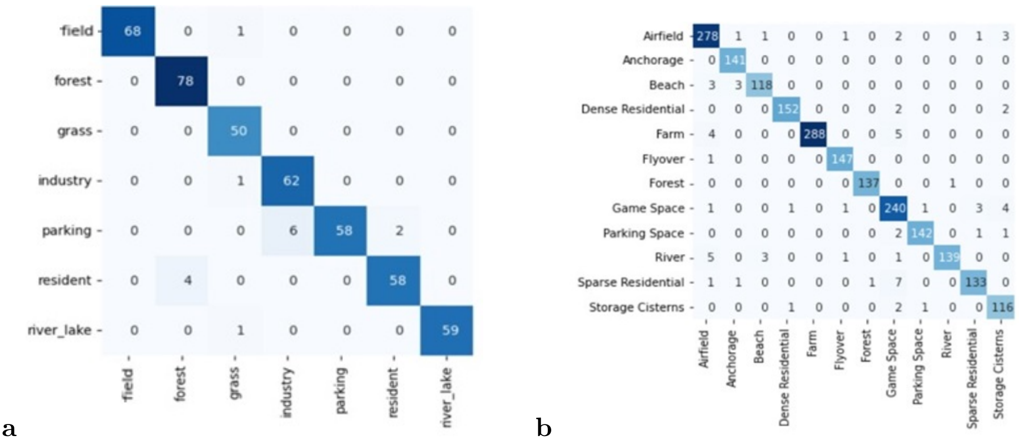

Fig. 11. DenseNet confusion matrix for the classification result for (**a**) RSSCN7 dataset; (**b**) NWPU-RESISC45 dataset.

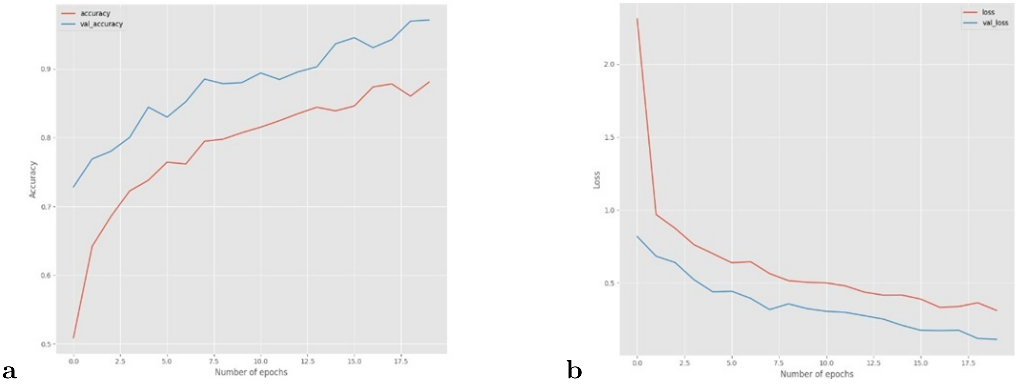

Fig. 12. Training model accuracy and loss plot graphs on RSSCN7 using InceptionV3. (**a**) Accuracy plot graph; (**b**) Loss plot graph.

The ensemble model performed exceptionally well in predicting the labels for these images. Fig. 14 shows the training model accuracy and loss plot graphs on RSSCN7 using InceptionV3.

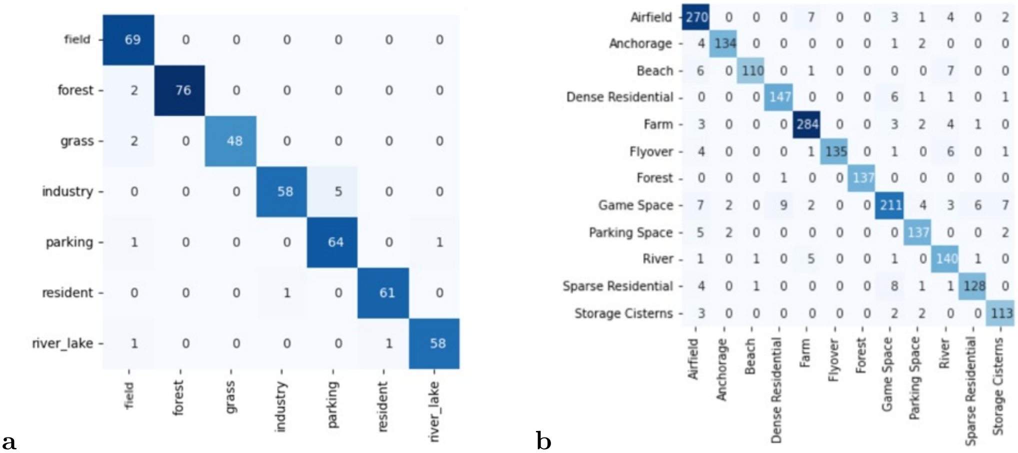

a

	field	forest	grass	industry	parking	resident	river_lake
field	69	0	0	0	0	0	0
forest	2	76	0	0	0	0	0
grass	2	0	48	0	0	0	0
industry	0	0	0	58	5	0	0
parking	1	0	0	0	64	0	1
resident	0	0	0	1	0	61	0
river_lake	1	0	0	0	0	1	58

b

	Airfield	Anchorage	Beach	Dense Residential	Farm	Flyover	Forest	Game Space	Parking Space	River	Sparse Residential	Storage Cisterns
Airfield	270	0	0	0	7	0	0	3	1	4	0	2
Anchorage	4	134	0	0	0	0	0	1	2	0	0	0
Beach	6	0	110	0	1	0	0	0	0	7	0	0
Dense Residential	0	0	0	147	0	0	0	6	1	1	0	1
Farm	3	0	0	0	284	0	0	3	2	4	1	0
Flyover	4	0	0	0	1	135	0	1	0	6	0	1
Forest	0	0	0	1	0	0	137	0	0	0	0	0
Game Space	7	2	0	9	2	0	0	211	4	3	6	7
Parking Space	5	2	0	0	0	0	0	0	137	0	0	2
River	1	0	1	0	5	0	0	1	0	140	1	0
Sparse Residential	4	0	1	0	0	0	0	8	1	1	128	0
Storage Cisterns	3	0	0	0	0	0	0	2	2	0	0	113

Fig. 13. InceptionV3 confusion matrix for the classification result for: (**a**) RSSCN7 dataset; (**b**) NWPU-RESISC45 dataset.

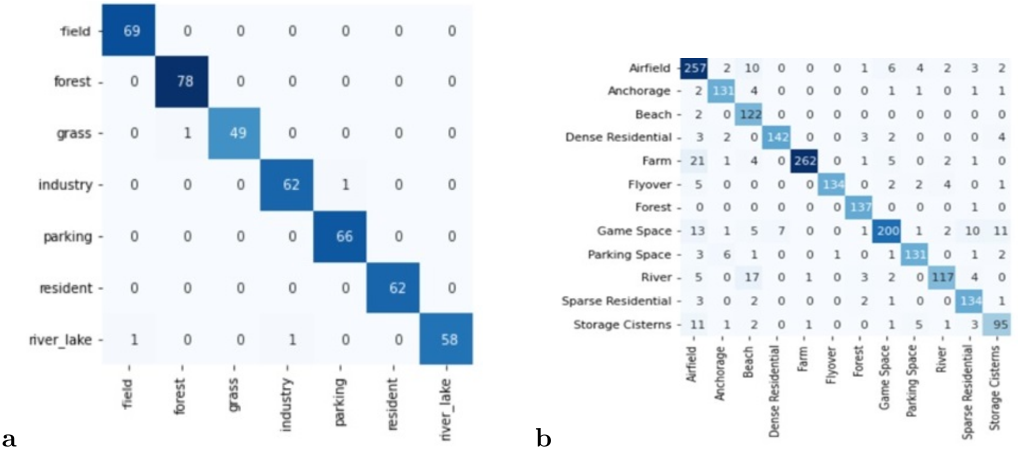

a

	field	forest	grass	industry	parking	resident	river_lake
field	69	0	0	0	0	0	0
forest	0	78	0	0	0	0	0
grass	0	1	49	0	0	0	0
industry	0	0	0	62	1	0	0
parking	0	0	0	0	66	0	0
resident	0	0	0	0	0	62	0
river_lake	1	0	0	1	0	0	58

b

	Airfield	Anchorage	Beach	Dense Residential	Farm	Flyover	Forest	Game Space	Parking Space	River	Sparse Residential	Storage Cisterns
Airfield	257	2	10	0	0	0	1	6	4	2	3	2
Anchorage	2	131	4	0	0	0	0	1	1	0	1	1
Beach	2	0	122	0	0	0	0	0	0	0	0	0
Dense Residential	3	2	0	142	0	0	3	2	0	0	0	4
Farm	21	1	4	0	262	0	1	5	0	2	1	0
Flyover	5	0	0	0	0	134	0	2	2	4	0	1
Forest	0	0	0	0	0	0	137	0	0	0	1	0
Game Space	13	1	5	7	0	0	1	200	1	2	10	11
Parking Space	3	6	1	0	0	1	0	1	131	0	1	2
River	5	0	17	0	1	0	3	2	0	117	4	0
Sparse Residential	3	0	2	0	0	0	2	1	0	0	134	1
Storage Cisterns	11	1	2	0	1	0	0	1	5	1	3	95

Fig. 14. Ensemble Confusion matrix for the classification result for: (**a**) RSSCN7 dataset; (**b**) NWPU-RESISC45 dataset.

4.5. Ensemble technique results comparision and analysis

In this study on aerial image classification, TL and ensemble models were employed to achieve high accuracy. Three individual models, VGG16, Densenet201, and InceptionV3, were evaluated, and an ensemble approach was utilized. Results showed that Densenet201 achieved an accuracy of 97.1%, while InceptionV3 performed even better

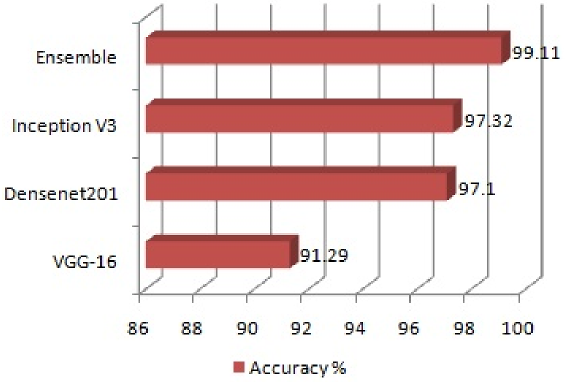

Fig. 15. Accuracy comparison graph for RSSCN7 dataset.

with 97.32%. VGG16, although slightly worse, still attained a respectable accuracy of 91.29%. Fig. 15 shows the graph depicting the compared models.

The ensemble approach, combining all three models, yielded a remarkable accuracy of 99.11%. These findings highlight the effectiveness of TL in improving classification accuracy, with InceptionV3 being the most successful individual model. The ensemble approach demonstrated its strength by surpassing the accuracy of all individual models. Overall, this research contributes to the advancement of aerial imagery study, delivering significant insights for various applications such as urban planning, environmental monitoring, and agriculture.

5. Conclusion and future scope

The various RS classification techniques are fully described in this paper, along with the study fields where they are used. The different algorithms employed in the classification and clustering of the RS images and how this data is compiled for the learning process are also covered in detail. It also goes into great depth on how to extract features from remote-sensing images using a CNN Model. This study has developed a DL-based classification method for RSSCN7 and NWPU-RESISC45 datasets with multiscene classes. The analysis of these datasets using Gabor filters and TL has achieved high accuracy in classifying diverse forms of aerial view scenes. Specifically, VGG16 attained an accuracy of 94%, DenseNet201 achieved 97%, and InceptionV3 also had 97%. These high levels of accuracy suggest that the Gabor filters and DL models are efficient in mining important attributes from aerial view images and accurately classifying them. An ensemble model built with these 3 models was also evaluated with sample test data. The accuracy, kappa coefficient, F1 score, and confusion matrix have all been used to verify the performance of the suggested approaches. The results revealed that the ensemble model obtained the best overall accuracy (99.11%) and kappa coefficient (0.99), while also improving the precision of river samples by 4%, respectively. The model's accuracy is valuable for a range of applications, such as RS, weather forecasting, and environmental monitoring. By identifying various aerial view scenes with high accuracy, the model offers effective intuitions into ecological surroundings, that would aid to inform decision-making processes. For instance, the model can help predict weather patterns, monitor air quality, and assess changes in environmental conditions.

Further research and testing will be necessary to evaluate the model's generalizability and robustness across different datasets and image categories. It's important to note that the model's performance is limited to the specific dataset and image categories utilized in the analysis. It might not generalize appropriately to new datasets or different types of aerial view scenes. Therefore, further research is needed to test the model's robustness and generalizability across different datasets and applications. The sample size and scope of the study could be increased, as well as the variation in aerial view scenes captured. Additionally, the study focused on the accuracy of the model, but it is also important to consider other performance metrics to gain a more complete insight of the model's effectiveness. Future extensions could include fine-tuning individual pre-trained networks. We also need to look into new methods and systems which may be utilised to deploy the combination of RS information from social media, and spatial technology in order to advance the state-of-the-art of RS image scene categorization.

References

[1] S. Abraham, A. Aniyan, A. Kembhavi, and N. Philip. Detection of bars in galaxies using a deep convolutional neural network. *Monthly Notices of the Royal Astronomical Society* 477(1):894–903. 2017. doi:10.1093/mnras/sty627.

[2] H. S. Alhichri, A. S. Alswayed, Y. Bazi, N. Ammour, and N. A. Alajlan. Classification of remote sensing images using EfficientNet-B3 CNN model with attention. *IEEE Access* 9:14078–14094. 2021. doi:10.1109/ACCESS.2021.3051085.

[3] M. Belgiu and L. Drăguţ. Random forest in remote sensing: A review of applications and future directions. *ISPRS Journal of Photogrammetry and Remote Sensing* 114:24–31. 04 2016. doi:10.1016/j.isprsjprs.2016.01.011.

[4] G. Cheng, D. Gao, Y. Liu, and J. Han. Multi-scale and discriminative part detectors based features for multi-label image classification. In: *Proceedings of the Twenty-Seventh International Joint Conference on Artificial Intelligence, IJCAI-18*, pp. 649–655. 2018. doi:10.24963/ijcai.2018/90.

[5] G. Cheng, J. Han, and X. Lu. Remote sensing image scene classification: Benchmark and state of the art. *Proceedings of the IEEE* 105:1865–1883. 04 2017. doi:10.1109/JPROC.2017.2675998.

[6] G. Cheng, X. Xie, J. Han, K. Li, and G.-S. Xia. Remote sensing image scene classification meets deep learning: Challenges, methods, benchmarks, and opportunities. *IEEE Journal of Selected Topics in Applied Earth Observations and Remote Sensing* 13:3735–3756. 2020. doi:10.1109/JSTARS.2020.3005403.

[7] G. Cheng, C. Yang, X. Yao, K. Li, and J. Han. When deep learning meets metric learning: Remote sensing image scene classification via learning discriminative CNNs. *IEEE Transactions on Geoscience and Remote Sensing* 56(5):2811–2821. 2018. doi:10.1109/TGRS.2017.2783902.

[8] B. Cui, X. Chen, and Y. Lu. Semantic segmentation of remote sensing images using transfer learning and deep convolutional neural network with dense connection. *IEEE Access* 8:116744–116755. 2020. doi:10.1109/ACCESS.2020.3003914.

[9] B. Demir and L. Bruzzone. A novel active learning method in relevance feedback for content-based remote sensing image retrieval. *IEEE Transactions on Geoscience and Remote Sensing* 53(5):2323–2334. 2015. doi:10.1109/TGRS.2014.2358804.

[10] I. Goodfellow, J. Pouget-Abadie, M. Mirza, B. Xu, D. Warde-Farley, et al. Generative adversarial networks. *Communications of the ACM* 63(11):139–144. 2020. doi:10.1145/3422622.

[11] G. Gui, H. Huang, Y. Song, and H. Sari. Deep learning for an effective non-orthogonal multiple access scheme. *IEEE Transactions on Vehicular Technology* 67(9):8440–8450. 2018. doi:10.1109/TVT.2018.2848294.

[12] Y. Hua, L. Mou, and X. Zhu. Recurrently exploring class-wise attention in a hybrid convolutional and bidirectional LSTM network for multi-label aerial image classification. *ISPRS Journal of Photogrammetry and Remote Sensing* 149:188–199. 2019. doi:10.1016/j.isprsjprs.2019.01.015.

[13] Y. Hua, L. Mou, and X. X. Zhu. Relation network for multilabel aerial image classification. *IEEE Transactions on Geoscience and Remote Sensing* 58(7):4558–4572. 2020. doi:10.1109/TGRS.2019.2963364.

[14] H. Huang, Y. Peng, J. Yang, W. Xia, and G. Gui. Fast beamforming design via deep learning. *IEEE Transactions on Vehicular Technology* 69(1):1065–1069. 2019. doi:10.1109/TVT.2019.2949122.

[15] H. Huang, J. Yang, Y. Song, H. Huang, and G. Gui. Deep learning for super-resolution channel estimation and doa estimation based massive mimo system. *IEEE Transactions on Vehicular Technology* 67(9):8549–8560. 2018. doi:10.1109/TVT.2018.2851783.

[16] H. Jiang, D. Zhao, Y. Cai, and S. An. A method for application of classification tree models to map aquatic vegetation using remotely sensed images from different sensors and dates. *Sensors* 12(9):12437–12454. 2012. doi:10.3390/s120912437.

[17] Z. Karim and T. van Zyl. Deep learning and transfer learning applied to sentinel-1 dinsar and sentinel-2 optical satellite imagery for change detection. In: *2020 International SAUPEC/RobMech/PRASA Conference*, pp. 1–7. 2020. doi:10.1109/SAUPEC/RobMech/PRASA48453.2020.9041139.

[18] N. Kato, Z. Fadlullah, B. Mao, F. Tang, O. Akashi, et al. The deep learning vision for heterogeneous network traffic control: Proposal, challenges, and future perspective. *IEEE Wireless Communications* 24(3):146–153. 2017. doi:10.1109/MWC.2016.1600317WC.

[19] N. Khan, U. Chaudhuri, B. Banerjee, and S. Chaudhuri. Graph convolutional network for multi-label vhr remote sensing scene recognition. *Neurocomputing* 357:36–46. 2019. doi:10.1016/j.neucom.2019.05.024.

[20] W. Li, H. Liu, Y. Wang, L. Zhuangzhuang, Y. Jia, et al. Deep learning-based classification methods for remote sensing images in urban built-up areas. *IEEE Access* 7:36274–36284. 2019. doi:10.1109/ACCESS.2019.2903127.

[21] W. Li, Z. Wang, Y. Wang, J. Wu, J. Wang, et al. Classification of high-spatial-resolution remote sensing scenes method using transfer learning and deep convolutional neural network. *IEEE Journal of Selected Topics in Applied Earth Observations and Remote Sensing* 13:1986–1995. 2020. doi:10.1109/JSTARS.2020.2988477.

[22] H. Liu, X. Huang, F. Han, J. Cui, B. Spencer, et al. Hybrid polarimetric GPR calibration and elongated object orientation estimation. *IEEE Journal of Selected Topics in Applied Earth Observations and Remote Sensing* 13:1986–1995. 2019. doi:10.1109/JSTARS.2019.2912339.

[23] H. Liu, H. Xia, M. Zhuang, Z. Long, C. Liu, et al. Reverse time migration of acoustic waves for imaging based defects detection for concrete and CFST structures. *Mechanical Systems and Signal Processing* 117:210–220. 2019. doi:10.1016/j.ymssp.2018.07.011.

[24] B. Mao, F. Tang, Z. Fadlullah, N. Kato, O. Akashi, et al. A novel non-supervised deep-learning-based network traffic control method for software defined wireless networks. *IEEE Wireless Communications* 25(4):74–81. 2018. doi:10.1109/MWC.2018.1700417.

[25] M. Mesvari and R. Shah-Hosseini. Segmentation of electrical substations using deep convolutional neural network. *ISPRS Annals of the Photogrammetry, Remote Sensing and Spatial Information Sciences* X-4/W1-2022:495–500. 2023. doi:10.5194/isprs-annals-X-4-W1-2022-495-2023.

[26] G. Mountrakis, J. Im, and C. Ogole. Support vector machines in remote sensing: A review. *ISPRS Journal of Photogrammetry and Remote Sensing* 66(3):247–259. 2011. doi:10.1016/j.isprsjprs.2010.11.001.

[27] F. A. Oliehoek, R. Savani, J. Gallego-Posada, E. Van der Pol, E. D. De Jong, et al. GANGs: Generative adversarial network games. arXiv, arXiv:1712.00679. 2017. doi:10.48550/arXiv.1712.00679.

[28] B. Petrovska, E. Zdravevski, P. Lameski, R. Corizzo, I. Štajduhar, et al. Deep learning for feature extraction in remote sensing: A case-study of aerial scene classification. *Sensors* 20(14):3906. 2020. doi:10.3390/s20143906.

[29] D. F. Santos, R. G. Pires, L. A. Passos, and J. P. Papa. DDIPNet and DDIPNet+: Discriminant deep image prior networks for remote sensing image classification. In: *2021 IEEE International Geoscience and Remote Sensing Symposium IGARSS*, pp. 2843–2846. 2021. doi:10.1109/IGARSS47720.2021.9554277.

[30] Z. Shao, J. Cai, P. Fu, L. Hu, and T. Liu. Deep learning-based fusion of Landsat-8 and Sentinel-2 images for a harmonized surface reflectance product. *Remote Sensing of Environment* 235:111425. 2019. doi:10.1016/j.rse.2019.111425.

[31] Z. Shao, W. Zhou, X. Deng, M. Zhang, and Q. Cheng. Multilabel remote sensing image retrieval based on fully convolutional network. *IEEE Journal of Selected Topics in Applied Earth Observations and Remote Sensing* 13:318–328. 2020. doi:10.1109/JSTARS.2019.2961634.

[32] R. Stivaktakis, G. Tsagkatakis, and P. Tsakalides. Deep learning for multilabel land cover scene categorization using data augmentation. *IEEE Geoscience and Remote Sensing Letters* 16(7):1031–1035. 2019. doi:10.1109/LGRS.2019.2893306.

[33] F. Tang, Z. Fadlullah, B. Mao, and N. Kato. An intelligent traffic load prediction based adaptive channel assignment algorithm in SDN-IoT: A deep learning approach. *IEEE Internet of Things Journal* 5(6):5141–5154. 2018. doi:10.1109/JIOT.2018.2838574.

[34] R. Verma and J. Ali. A comparative study of various types of image noise and efficient noise removal techniques. *International Journal of Advanced Research in Computer Science and Software Engineering* 3:617–622. 2013.

[35] Y. Wang, M. Liu, J. Yang, and G. Gui. Data-driven deep learning for automatic modulation recognition in cognitive radios. *IEEE Transactions on Vehicular Technology* 68(4):4074–4077. 2019. doi:10.1109/TVT.2019.2900460.

[36] B. Xia, F. Kong, J. Zhou, X. Wu, and Q. Xie. Land resource use classification using deep learning in ecological remote sensing images. *Computational Intelligence and Neuroscience* 2022:7179477. 2022. doi:10.1155/2022/7179477.

[37] Y. Zhong, X. Han, and L. Zhang. Multi-class geospatial object detection based on a position-sensitive balancing framework for high spatial resolution remote sensing imagery. *ISPRS Journal of Photogrammetry and Remote Sensing* 138:281–294. 2018. doi:10.1016/j.isprsjprs.2018.02.014.

[38] X. X. Zhu, D. Tuia, L. Mou, G.-S. Xia, L. Zhang, et al. Deep learning in remote sensing: A comprehensive review and list of resources. *IEEE Geoscience and Remote Sensing Magazine* 5(4):8–36. 2017. doi:10.1109/MGRS.2017.2762307.

[39] Q. Zou, L. Ni, T. Zhang, and Q. Wang. Deep learning based feature selection for remote sensing scene classification. *IEEE Geoscience and Remote Sensing Letters* 12(11):2321–2325. 2015. doi:10.1109/LGRS.2015.2475299.

K Aditya Shastry completed his Ph.D. in Computer Science and Engineering in 2019 from VTU, India. He completed his B.E. in 2000 and M.Tech. in 2007. He has more than three years of industry experience and 20+ years of teaching experience. He has authored numerous papers in reputed journals and conferences. He has more than 10 book chapters to his credit that are published by reputed publishers. He has given many invited talks as a resource person. He is also a reviewer of reputed journals. To his credit, he has two funded projects from VGST and ISRO. His areas of interest include machine learning, deep learning, and data mining. Currently he is working as Professor in the Department of Information Science and Engineering at Nitte Meenakshi Institute of Technology, Bengaluru, India.

Reshma Itagi received her master's degree from Nitte Meenakshi Institute of Technology, India. She is now a software engineer at Harman, specializing in full-stack development. Her main research interests include machine learning, deep learning, and data analytics.